

Data-driven Regularization via Racecar Training for Generalizing Neural Networks

You Xie Nils Thuerey
 you.xie@tum.de nils.thuerey@tum.de

Technical University of Munich
<https://github.com/tum-pbs/racecar>

Abstract

We propose a novel training approach for improving the generalization in neural networks. We show that in contrast to regular constraints for orthogonality, our approach represents a *data-dependent* orthogonality constraint, and is closely related to singular value decompositions of the weight matrices. We also show how our formulation is easy to realize in practical network architectures via a reverse pass, which aims for reconstructing the full sequence of internal states of the network. Despite being a surprisingly simple change, we demonstrate that this forward-backward training approach, which we refer to as *racecar* training, leads to significantly more generic features being extracted from a given data set. Networks trained with our approach show more balanced mutual information between input and output throughout all layers, yield improved explainability and, exhibit improved performance for a variety of tasks and task transfers.

1 Introduction

Despite their vast success, training neural networks that generalize well to a wide range of previously unseen tasks remains a fundamental challenge [35, 26, 2, 13]. A variety of techniques have been proposed over the years, ranging from well-established ones like dropout [44], and weight decay [33, 20, 52, 30], to techniques for orthogonalization [37, 25, 2]. While the former ones primarily focus on avoiding over-fitting rather than generality, the latter is closer to the goals of our paper: generalization is often seen in terms of extracting the most basic set of feature templates [45], similar to orthogonal vectors, that span the distribution of a data set under consideration. Here,

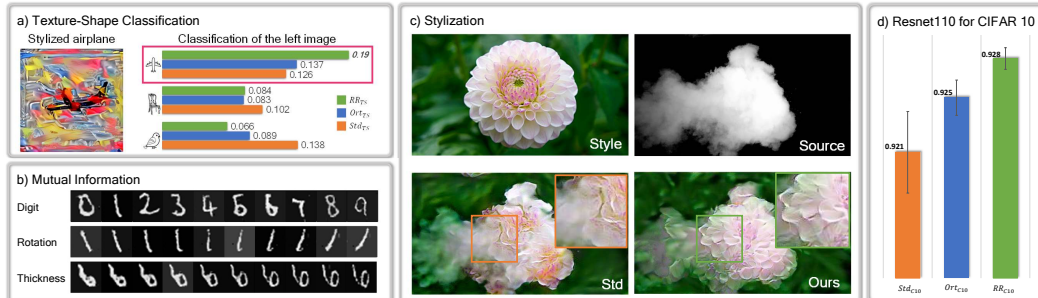


Figure 1: Racecar training yields improved results for a wide range of applications: **a)** For difficult shape classification tasks, our approach outperforms regular training (Std_{TS}) as well as state-of-the-art regularizers (Ort_{TS}): the RR_{TS} model instead classifies the airplane shape with high confidence. **b)** Our approach establishes mutual information between input and output distributions, retrieving intuitive and explainable dimensions. **c)** A racecar model yields an improved reconstruction for stylization tasks. **d)** For CIFAR 10 classification with a Resnet110, RR_{C10} yields substantial practical improvements over the state-of-the-art Ort_{C10} .

especially the dominant features [38] that occur most often in a data set are those that have the highest potential to be applicable in new contexts and yield generalizing capabilities. The challenge of extracting such features is two-fold: finding the dominant features in a large and diverse data-set, and representing them given limited computational resources. Our formulation incurs only a very moderate computational cost, is very easy to integrate and widely applicable, while at the same time outperforming existing methods for extracting dominant features.

Our formulation draws inspiration from the human trait to disassemble and re-assemble objects. These deconstruction tasks serve a wide range of purposes, from a hobby for motorists, to an essential source of learning and exploration for children [19]. We show that dominant, and general features can be learned with a simple, yet powerful and general modification of neural network training in line with these re-assembly tasks: in addition to a regular forward pass, we add a reverse pass that is constrained to reconstruct all in-between results of the forward pass as well as the input. This palindromic structure yields substantial improvements for generalization of the learned representations in a wide range of architectures and significantly improves performance. Our results indicate that the reversible nature of the proposed training setup, which we will subsequently refer to via the palindrome "racecar" due to the backward-forward connectivity of the resulting network, encourages the learning of generic and reusable features that benefit a wide range of objectives.

We will evaluate the generality of the extracted dominant features in the context of transfer learning. For a regular, i.e., a non-transfer task, the goal usually is to train a network that gives the optimal performance for one specific goal. This has been demonstrated in numerous success stories [32, 29, 17, 21]. In a regular training run, the network naturally exploits any observed correlations between input and output distribution. E.g., if the color of an object in any way correlates with its type, the training of a classifier should find and use this information. In recent years, even networks trained only for a very specific task were shown to be surprisingly suitable starting points when training models for different tasks [54, 18, 8]. Often, the original network learned representations that were at least partially applicable to different data domains. An inherent difficulty in this setting is that typically no knowledge about the specifics of the new data and task domains is available at the training time of the source model. While it is common practice to target broad and difficult tasks hoping that this will result in features that are applicable in new domains, we instead leverage the data distribution of the inputs when training the source model.

The structure of our networks is inspired by invertible network architectures that have received significant attention in recent years [16, 24, 56]. However, instead of aiming for a bijective mapping that reproduces inputs, we strive for learning a general representation by constraining the network to represent an as-reversible-as-possible process for all *intermediate* layer activations. Thus, even for cases where a classifier can, e.g., rely on color for inference of an object type, the model is encouraged to learn a representation that can recover the input. Hence, not only the color of the input should be retrieved, but also, e.g., its shape. In contrast to most structures for invertible networks, racecar training does not impose architectural restrictions. We demonstrate the benefits of racecar training for a variety of architectures, from fully connected layers to convolutional neural networks (CNNs), over networks with and without batch normalization, to GAN architectures.

2 Related Work

Several prior methods employed "hard orthogonal constraints" to improve weight orthogonality via singular value decomposition (SVD) at training time [23, 25, 37]. Bansal et al. [2] additionally investigated efficient formulations of the orthogonality constraints. In practice, these constraints are difficult to satisfy, and correspondingly only weakly imposed. Besides, these methods focus on improving performance for a known, given task. This means the training process only extracts features that the network considers useful for improving the performance of the current task, not necessarily improving generalization or transfer performance [49]. While our racecar training shares similarities with SVD-based constraints, it can be realized with a very efficient L^2 -based formulation, and takes the full input distribution into account, leading to improved generalization.

Recovering all input information from hidden representations of a network is generally very difficult [9, 34], due to the loss of information throughout the layer transformations. In this context, [48] proposed the information bottleneck principle, which states that for an optimal representation, information unrelated to the current task is omitted. This highlights the common specialization of conventional training approaches. Reversed network architectures were proposed in previous work [1, 24, 16], but mainly focus on how to make a network fully invertible via augmenting the network

with special structures. As a consequence, the path from input to output is different from the reverse path that translates output to input. Besides, the augmented structures of these approaches can be challenging to apply to general network architectures. In contrast, our approach fully preserves an existing architecture for the backward path, and does not require any operations that were not part of the source network. As such, it can easily be applied in new settings, e.g., adversarial training [17]. While methods using reverse connections were previously proposed [56, 46], these modules primarily focus on transferring information between layers for a given task, and on auto-encoder structures for domain adaptation, respectively.

Transfer learning with deep neural networks has been very successful for a variety of challenging tasks, such as image classification [11, 31, 60], multi-language text classification [59, 39, 58], and medical imaging problems [40]. [54] proposed an approach to obtain task relationship graphs for different tasks. In this context, a central challenge is to set up the training process such that it leads to learning generic features from the data set, which are useful for both source and related tasks rather than specific features for the source task.

3 Method

Regularization via orthogonality has become a popular tool for training deep CNNs and was shown to improve performance [23, 2]. The corresponding constraints can be formulated as:

$$\mathcal{L}_{\text{ort}} = \sum_{m=1}^n \left\| M_m^T M_m - I \right\|_F^2, \quad (1)$$

i.e., enforcing the transpose of the weight matrix $M_m \in \mathbb{R}^{s_m^{\text{out}} \times s_m^{\text{in}}}$ for all layers m to yield its inverse when being multiplied with the original matrix. I denotes the identity matrix with $I = (\mathbf{e}_m^1, \dots, \mathbf{e}_m^{s_m^{\text{in}}})$, \mathbf{e}_m^j denoting the j th column unit vector. Minimizing Eq. (1), i.e. $M_m^T M_m - I = 0$ is mathematically equivalent to:

$$M_m^T M_m \mathbf{e}_m^j - \mathbf{e}_m^j = \mathbf{0}, j = 1, 2, \dots, s_m^{\text{in}}, \quad (2)$$

with $\text{rank}(M_m^T M_m) = s_m^{\text{in}}$, and \mathbf{e}_m^j as eigenvectors of $M_m^T M_m$ with eigenvalues of 1. This formulation highlights that Eq. (2) does not depend on the training data, and instead only targets the content of M_m . Our approach re-formulates the original orthogonality constraint in a *data-driven* manner: we take into account the set \mathcal{D}_m of inputs for the current layer (either activation from a previous layer or the training data \mathcal{D}_1), and instead minimize

$$\mathcal{L}_{\text{RR}} = \sum_{m=1}^n (M_m^T M_m \mathbf{d}_m^i - \mathbf{d}_m^i)^2 = \sum_{m=1}^n ((M_m^T M_m - I) \mathbf{d}_m^i)^2, \quad (3)$$

where $\mathbf{d}_m^i \in \mathcal{D}_m \subset \mathbb{R}^{s_m^{\text{in}}}$. This re-formulation of orthogonality allows for minimizing the loss by extracting the dominant features of the input data instead of only focusing on the content of M_m .

We use q to denote the number of linearly independent entries in \mathcal{D}_m , i.e. its dimension, and t the size of the training data, i.e. $|\mathcal{D}_m| = t$, usually with $q < t$. For every single datum $\mathbf{d}_m^i, i = 1, 2, \dots, t$, Eq. (3) results in

$$M_m^T M_m \mathbf{d}_m^i - \mathbf{d}_m^i = \mathbf{0}, \quad (4)$$

and hence \mathbf{d}_m^i are eigenvectors of $M_m^T M_m$ with corresponding eigenvalues being 1. Thus, instead of the generic constraint $M_m^T M_m = I$ that is completely agnostic to the data at hand, the proposed formulation of Eq. (13) is aware of the training data, which improves the generality of the learned representation, as we will demonstrate in detail below.

As by construction, $\text{rank}(M_m) = r \leq \min(s_m^{\text{in}}, s_m^{\text{out}})$, the SVD of M_m yields:

$$M_m = U_m \Sigma_m V_m^T, \text{ with } \begin{cases} U_m = (\mathbf{u}_m^1, \mathbf{u}_m^2, \dots, \mathbf{u}_m^r, \mathbf{u}_m^{r+1}, \dots, \mathbf{u}_m^{s_m^{\text{out}}}) \in \mathbb{R}^{s_m^{\text{out}} \times s_m^{\text{out}}}, \\ V_m = (\mathbf{v}_m^1, \mathbf{v}_m^2, \dots, \mathbf{v}_m^r, \mathbf{v}_m^{r+1}, \dots, \mathbf{v}_m^{s_m^{\text{in}}}) \in \mathbb{R}^{s_m^{\text{in}} \times s_m^{\text{in}}}, \end{cases} \quad (5)$$

with left and right singular vectors in U_m and V_m , respectively, and Σ_m having square roots of the r eigenvalues of $M_m^T M_m$ on its diagonal. \mathbf{u}_m^k and $\mathbf{v}_m^k (k = 1, \dots, r)$ are the eigenvectors of $M_m M_m^T$ and $M_m^T M_m$, respectively [50]. Here, especially the right singular vectors in V_m^T are important, as they determine which structures of the input are processed by the transformation M_m . The original orthogonality constraint with Eq. (2) yields r unit vectors \mathbf{e}_m^j as the eigenvectors of $M_m^T M_m$. Hence, the influence of Eq. (2) on V_m is completely independent of training data and learning objectives.

Next, we show that \mathcal{L}_{RR} facilitates learning dominant features from a given data set. For this, we consider an arbitrary basis to span the space of inputs \mathcal{D}_m for layer m . Let $\mathcal{B}_m : \langle \mathbf{w}_m^1, \dots, \mathbf{w}_m^q \rangle$ denote a set of q orthonormal basis vectors obtained via a Gram-Schmidt process, with $t \geq q \geq r$, and D_m denoting the matrix of the vectors in \mathcal{B}_m . As we show in more detail in the appendix, our constraint from Eq. (13) requires eigenvectors of $M^T M$ to be \mathbf{w}_m^i , with V_m containing r orthogonal vectors $(\mathbf{v}_m^1, \mathbf{v}_m^2, \dots, \mathbf{v}_m^r)$ from \mathcal{D}_m and $(s_m^{\text{in}} - r)$ vectors from the null space of M .

We are especially interested in how M_m changes w.r.t. input in terms of D_m , i.e., we express \mathcal{L}_{RR} in terms of D_m . By construction, each input \mathbf{d}_m^i can be represented as a linear combination via a vector of coefficients \mathbf{c}_m^i that multiplies D_m so that $\mathbf{d}_m^i = D_m \mathbf{c}_m^i$. Since $M_m \mathbf{d}_m = U_m \Sigma_m V_m^T \mathbf{d}_m$, the loss \mathcal{L}_{RR} of layer m can be rewritten as

$$\begin{aligned} \mathcal{L}_{RR_m} &= (M_m^T M_m \mathbf{d}_m - \mathbf{d}_m)^2 = (V_m \Sigma_m^T \Sigma_m V_m^T \mathbf{d}_m - \mathbf{d}_m)^2 \\ &= (V_m \Sigma_m^T \Sigma_m V_m^T D_m \mathbf{c}_m - D_m \mathbf{c}_m)^2, \end{aligned} \quad (6)$$

where we can assume that the coefficient vector \mathbf{c}_m is accumulated over the training data set size t via $\mathbf{c}_m = \sum_{i=1}^t \mathbf{c}_m^i$, since eventually every single datum in \mathcal{D}_m will contribute to \mathcal{L}_{RR_m} . The central component of Eq. (6) is $V_m^T D_m$. For a successful minimization, V_m needs to retain those \mathbf{w}_m^i with the largest \mathbf{c}_m coefficients. As V_m is typically severely limited in terms of its representational capabilities by the number of adjustable weights in a network, it needs to focus on the most important eigenvectors in terms of \mathbf{c}_m in order to establish a small distance to $D_m \mathbf{c}_m$. Thus, features that appear multiple times in the input data with a corresponding factor in \mathbf{c}_m will more strongly contribute to minimizing \mathcal{L}_{RR_m} .

To summarize, V_m is driven towards containing r orthogonal vectors \mathbf{w}_m^i that represent the most frequent features of the input data, i.e., the dominant features. Additionally, due to the column vectors of V_m being mutually orthogonal, M_m is encouraged to extract different features from the input. By the sake of being distinct and representative for the data set, these features have the potential to be useful for new inference tasks. The feature vectors embedded in M_m can be extracted from the network weights in practical settings, as we will demonstrate below.

Realization in Neural Networks Calculating $M_m^T M_m$ is usually very expensive due to the dimensionality of M_m . Instead of building it explicitly, we constrain intermediate results to realize Eq. (3) when training. A regular training typically starts with a chosen network structure and trains the model weights for a given task via a suitable loss function. Our approach fully retains this setup and adds a second pass that reverses the initial structure while reusing all weights and biases. E.g., for a typical fully connected layer in the forward pass with $\mathbf{d}_{m+1} = M_m \mathbf{d}_m + \mathbf{b}_m$, the reverse pass operation is given by $\mathbf{d}'_m = M_m^T (\mathbf{d}_{m+1} - \mathbf{b}_m)$, where \mathbf{d}'_m denotes the reconstructed input.

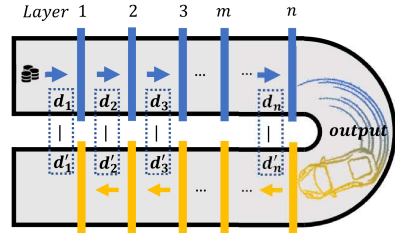


Figure 2: A visual overview of the regular forward pass (blue) and the corresponding reverse pass (yellow) that we employ to learn via data-dependent orthogonality constraints.

Our goal with the reverse pass is to transpose all operations of the forward pass to obtain identical intermediate activations between the layers with matching dimensionality. We can then constrain the intermediate results of each layer of the forward pass to match the results of the backward pass, as illustrated in Fig. 12. Due to the symmetric structure of the two passes, we can use a simple L^2 difference to drive the network towards aligning the results:

$$\mathcal{L}_{\text{racecar}} = \sum_{m=1}^n \lambda_m \left\| \mathbf{d}_m - \mathbf{d}'_m \right\|_F^2. \quad (7)$$

Here \mathbf{d}_m denotes the input of layer m in the forward pass and \mathbf{d}'_m the output of layer m for the reverse pass. λ_m denotes a scaling factor for the loss of layer m , which, however, is typically constant in our tests across all layers. Note that with our notation, \mathbf{d}_1 and \mathbf{d}'_1 refer to the input data, and the reconstructed input, respectively.

Next, we show how this setup realizes the regularization from Eq. (3). For clarity, we use a fully connected layer with bias. In a neural network with n hidden layers, the forward process for a layer m is given by:

$$\mathbf{d}_{m+1} = M_m \mathbf{d}_m + \mathbf{b}_m, \quad (8)$$

with \mathbf{d}_1 and \mathbf{d}_{n+1} denoting in- and output, respectively. For racecar training, we build a layer-wise reverse pass network with transposed operations and intermediate results \mathbf{d}_{m+1} :

$$\mathbf{d}'_m = M_m^T(\mathbf{d}_{m+1} - \mathbf{b}_m), \quad (9)$$

which yields $\|\mathbf{d}_m - \mathbf{d}'_m\|_F^2 = M_m^T M_m \mathbf{d}_m - \mathbf{d}_m$. When this difference is minimized via Eq. (7), we obtain activated intermediate content during the reverse pass that reconstructs the values computed in the forward pass, i.e. $\mathbf{d}'_{m+1} = \mathbf{d}_{m+1}$ holds. Replacing \mathbf{d}_{m+1} with \mathbf{d}'_{m+1} in Eq. (9), yields a full reverse pass from output to input, which we use most racecar training runs below. This version is preferable if a unique path from output to input exists. For architectures where the path is not unique, e.g., in the presence of additive residual connections, we use the layer-wise formulation from Eq. (9). The full formulation instead gives:

$$\mathbf{d}'_m = M_m^T(\mathbf{d}'_{m+1} - \mathbf{b}_m) = M_m^T(\mathbf{d}_{m+1} - \mathbf{b}_m) = M_m^T M_m \mathbf{d}_m, \quad (10)$$

which is consistent with Eq. (3), and hence satisfies the original constraint $M_m^T M_m \mathbf{d}_m - \mathbf{d}_m = \mathbf{0}$. Up to now, the discussion focused on simplified neural networks without activation functions or extensions such as batch normalization (BN). While we leave incorporating such extensions into the derivation for future work, our experiments consistently show that the inherent properties of racecar training remain valid: even with activations and BN, our approach successfully extracts dominant structures and yields improved generalization. In the appendix, we give details on how to ensure that the latent space content for forward and reverse pass is aligned such that differences can be minimized.

To summarize, we realize the loss formulation of Eq. (7) to minimize $\sum_{m=1}^n ((M_m^T M_m - I)\mathbf{d}_m)^2$ without explicitly having to construct $M_m^T M_m$. We will refer to networks trained with the added reverse structure and the additional loss terms as being trained with *racecar training*. We consider two variants for the reverse pass: a layer-wise racecar training Eq. (9) using the local datum \mathbf{d}_{m+1} , and a full version via Eq. (10) which uses \mathbf{d}'_{m+1} .

Experiments We will use the following naming scheme to differentiate variants in the experiments below: **Std_T**, **RR_T**, **Ort_T** for base models trained for a task T. Here, **Std** denotes a regular training run (in orange color in graphs below), while **RR** denotes models trained with our racecar training (in green). While we typically use all layers of a network in the racecar constraints, a special reduced variant that we compare to below only applies the constraint for the input data, i.e., $m=1$ in our notation. A network trained with this variant, denoted by **RR_A¹**, is effectively trained to only reconstruct the input. It contains no constraints for the inner activations of the network. **Ort** additionally denotes models trained with Spectral Restricted Isometry Property (SRIP) orthogonal regularization [2] (in blue). We verify that the column vectors of V_m of models from racecar training contain the dominant features of the input with the help of two classification tests. Both cases employ a single hidden fully connected layer, i.e. $\mathbf{d}_2 = M_1 \mathbf{d}_1$. In the first MNIST test, the training data consists only of 2 different images. After training, we compute the SVD for M_1 . Qualitatively, **RR** shows v_m^i that have obvious similarity with the two inputs, while the vectors of **Std** and **Ort** contain no recognizable structures (Fig. 3a). To quantify this similarity, we compute an LPIPS distance [57] between v_m^i and the training data (lower values being better). These measurements confirm that the singular values of the **RR** model with 0.282 ± 0.82 are significantly more similar to the input images that **Std** and **Ort**, with 0.411 ± 0.05 and 0.403 ± 0.031 , respectively. For the second classification test, we employ a training data set that is constructed from two dominant classes (a peak in the top left, and bottom right quadrant, respectively), augmented with noise in the form of random scribbles. Based on the analysis above, we expect the racecar training to extract the two dominant peaks during training. Our results confirm this: the peaks are clearly visible for racecar training, an example is shown in Fig. 3(b), while the other models fail to extract structures that resemble the input. The LPIPS distances confirm the visual similarity with 0.217 ± 0.022 for **RR**, 0.500 ± 0.002 for **Std** and 0.495 ± 0.006 for **Ort**. Thus, our training approach yields a way for humans to inspect the structures learned by a neural network.

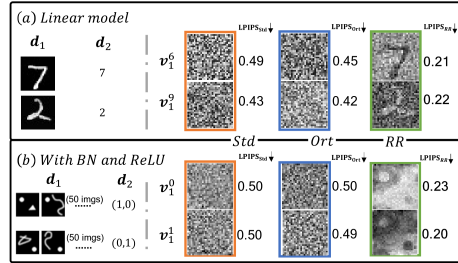


Figure 3: Column vectors of V_m for different trained models **Std**, **Ort** and **RR**: (a) MNIST and (b) for peaks. Input features clearly are successfully embedded in the weights of **RR**.

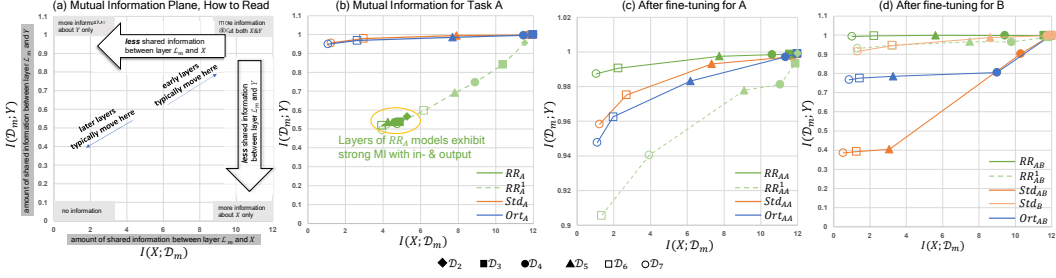


Figure 4: MI plane comparisons for different models. a) Visual overview of the content. b) Plane of task A. Points on each line correspond to layers of one type of model. All points of RR_A , are located in the center of the graph, while Std_A and Ort_A , exhibit large $I(\mathcal{D}_m; Y)$, i.e., specialize on the output. c,d): After fine-tuning for A/B. The last layer \mathcal{D}_7 of RR_{AA} builds the strongest relationship with Y .

The results above experimentally confirm our derivation of the racecar loss, and its ability to extract dominant and generalizing structures from the training data. We have focused on relatively simple setups here, as this allows us to quantify similarity via the training data. Our results below indicate that racecar training similarly extracts dominant structures from the activations for the deeper layers of a network. However, due to the lack of ground truth data, it is not easy to evaluate these structures. Thus, we turn to measurements in terms of mutual information in the next section.

The constraints of Eq. (7) intentionally only minimize differences in an averaged manner with an L^2 norm, as we don't strive for a perfectly bijective mapping between in- and output domains. Instead, racecar training aims at encouraging the network to extract dominant features that preserve as much information from the input data set as possible, given the representative capabilities of the chosen architecture. Hence, while regular training allows a model to specialize its extracted features to maximize performance for a given task, our approach considers the full data distribution of the input to represent its dominant features.

4 Evaluation in Terms of Mutual Information

As our approach hinges on the introduction of the reverse pass, we will show that it succeeds in terms of establishing mutual information (MI) between the input and the constrained intermediates inside a network. More formally, MI $I(X; Y)$ of random variables X and Y measures how different the joint distribution of X and Y is w.r.t. the product of their marginal distributions, i.e., the Kullback-Leibler divergence $I(X; Y) = D_{KL}[P_{(X,Y)} || P_X P_Y]$. [48] proposed *MI plane* to analyze trained models, which show the MI between the input X and activations of a layer \mathcal{D}_m , i.e., $I(X; \mathcal{D}_m)$ and $I(\mathcal{D}_m; Y)$, i.e., MI of layer \mathcal{D}_m with output Y . These two quantities indicate how much information about the in- and output distributions are retained at each layer, and we use them to show to which extent racecar training succeeds at incorporating information about the inputs throughout training.

The following tests employ networks with six fully connected layers with the objective to learn the mapping from 12 binary inputs to 2 binary output digits [42], with results accumulated over five runs. We compare the versions Std_A , Ort_A , RR_A , and a variant of the latter: RR_A^1 , i.e. a version where only the input \mathcal{d}_1 is constrained to be reconstructed. While Fig. 17 (a), visually summarizes the content of the MI planes, the graph in (b) highlights that racecar training correlates input and output distributions across all layers: the cluster of green points in the center of the graph shows that all layers contain balanced MI between in- as well as output and the activations of each layer. RR_A^1 fares slightly worse, while Std_A and Ort_A almost exclusively focus on the output with $I(\mathcal{D}_m; Y)$ being close to one. Once we continue fine-tuning these models without regularization, the MI naturally shifts towards the output, as shown in Fig. 17 (c). RR_{AA} outperforms others in terms of final performance. Likewise, RR_{AB} performs best for a transfer task B with switched output digits, as shown in graph (d). The final performance for both tasks across all runs is summarized in Fig. 5. It

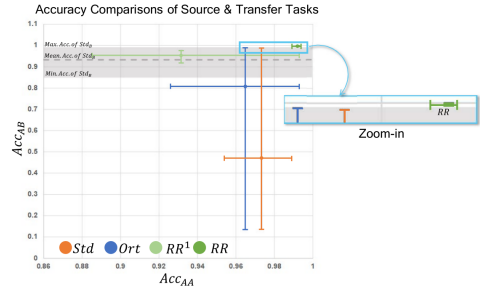


Figure 5: Performance for MI source and transfer tasks for the models of Fig. 17. Due to the large standard deviation of Ort , we show min/max value ranges. The dashed gray line and region show baseline accuracy for Std_B . The top-left inset highlights the stability of the high accuracy results from racecar training.

RR_{AA} outperforms others in terms of final performance. Likewise, RR_{AB} performs best for a transfer task B with switched output digits, as shown in graph (d). The final performance for both tasks across all runs is summarized in Fig. 5. It

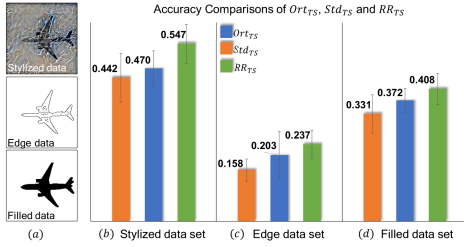


Figure 7: (a) Examples from texture-shape data set. (b, c, d) Texture-shape test accuracy comparisons of Ort_{TS} , Std_{TS} and RR_{TS} for different data sets.

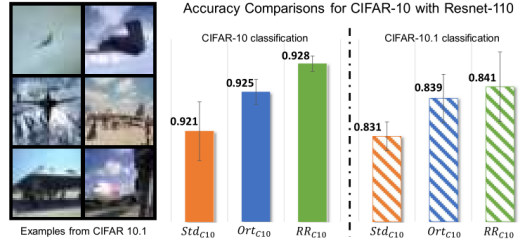


Figure 8: Left: Examples from CIFAR 10.1 data set. Right: Accuracy comparisons when applying models trained on CIFAR 10 to CIFAR 10.1 data.

is apparent that our approach gives the highest performance and very stable results. These graphs visualize that racecar training succeeds in robustly extracting reusable features.

MI has received attention recently as a learning objective, e.g., in the form of the InfoGAN approach [5] for learning disentangled and interpretable latent representations. Interestingly, a side-effect of the racecar training is that it successfully establishes mutual information between inputs and outputs, as shown in the previous paragraphs. And while MI is typically difficult to assess and estimate [51], our approach provides a simple and robust way for including it as a learning objective. In this way, we can, e.g., reproduce the disentangling results from [5], as shown in Fig. 11(c). A generative model with racecar training extracts intuitive latent dimensions for the different digits, line thickness, and orientation without any additional modifications of the loss function.

5 Experimental Results

To illustrate that racecar training is a practical approach that can be employed in real-world deep learning scenarios, we now turn to a broad range of complex network structures, i.e., CNNs, Autoencoders, and GANs, with a variety of data sets and tasks. We provide quantitative and qualitative results to show our approach succeeds in improving the generality of neural networks.

Transfer-learning Benchmarks We first evaluate our approach with two state-of-the-art transfer learning benchmark data sets. The first one uses the texture-shape data set from [15], which contains challenging images of various shapes combined with patterns and textures to be classified. The results below are given for 10 runs each. For the stylized data shown in Fig. 7 (a), Std_{TS} yields a performance of 44.2%, and Ort_{TS} improves the performance to 47.0%, while RR_{TS} yields a performance of 54.7% (see Fig. 7b). Thus, the accuracy of RR_{TS} is 23.76% higher than Std_{TS} , and 16.38% higher than Ort_{TS} . To assess generality, we also apply the models to new data without retraining, i.e. an edge and a filled data set, also shown in Fig. 7 (a). For the edge data set, RR_{TS} outperforms both Std_{TS} and Ort_{TS} by 50% and 16.75%, respectively. It is worth pointing out that the additional constraints of our racecar training lead to increased requirements for memory and additional computations, e.g., 41.86% more time per epoch than regular training for the texture-shape test. On the other hand, it allows us to train smaller models: we can reduce the weight count by 32% for the texture-shape case while still being on-par with Ort_{TS} in terms of classification performance.

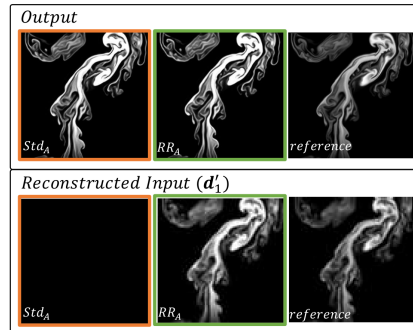


Figure 6: Example output and reconstructed low resolution results, with the reference shown right. Only RR_A successfully recovers the input. Std_A produces a black image.

As a second test case, we use a CIFAR-based task transfer [41] that measures how well models trained on the original CIFAR 10, generalize to a new data set (CIFAR 10.1) collected according to the same principles as the original one. Here we use a Resnet110 with 110 layers and 1.7 million parameters. In terms of accuracy across 5 runs, Ort_{C10} outperforms Std_{C10} by 0.39%, while RR_{C10} outperforms Ort_{C10} by another 0.28% in terms of absolute test accuracy (Fig. 24). This increase for racecar training matches the gains reported for orthogonality in previous work [2], and thus shows that our approach yields substantial practical improvements over the latter. It is especially interesting how well performance for CIFAR 10 translates into transfer performance for CIFAR 10.1. Here, RR_{C10} still outperforms Ort_{C10} and Std_{C10} by 0.22% and 0.95%, respectively. Hence, the models

from racecar training very successfully translate gains in performance from the original task to the new one, which indicates that the models have successfully learned a set of more general features. To summarize, both benchmark cases confirm that racecar training benefits generalization. As racecar training consistently outperforms orthogonalization, we focus on comparisons with regular training in the following.

Generative Adversarial Models In this section, we employ racecar training in the context of generative models for transferring from synthetic to real-world data from the ScalarFlow data set [12]. As super-resolution task A , we first use a fully-convolutional generator network, adversarially trained with a discriminator network on the synthetic flow data. Fig. 6 demonstrates that the racecar network structure works in conjunction with the GAN training. As shown in the bottom row, the trained generator succeeds in recovering the input via the reverse pass without modifications. A regular model Std_A , only yields a black image in this case.

We now mirror the generator model from the previous task to create an autoencoder structure that we apply to two different data sets: the synthetic smoke data used for the GAN training (task B_1), and a real-world RGB data set of smoke clouds (task B_2). Thus both variants represent transfer tasks, the second one being more difficult due to the changed data distribution. The resulting losses, summarized in Fig. 9, show that racecar training performs best for both autoencoder tasks: the L^2 loss of RR_{AB_1} is 68.88% lower than Std_{AB_1} for B_1 , and 13.3% lower for task B_2 . The latter is especially encouraging, as it represents a transfer from training with fully synthetic images to real-world images.

VGG19 Stylization To provide a qualitative evaluation in a complex visual scenario, we turn to image stylization. We use VGG₁₉ networks [43] with more than 142 million parameters [7], and train models with and without racecar training, i.e. RR and Std . Both networks are then used for stylization tasks [14]. As this task strongly depends on the features of the base network, it visualizes the differences of the learned structures.

Several results of such stylizations are shown in Fig. 11 and Fig. 10. While the former highlights improved reconstruction of the leaf structures of the flower, the latter shows the popular setup of transforming a horse into a zebra. In Fig. 10, the regular model has difficulties distinguishing the background and the horse, and inserts green patches into the body. In contrast, the VGG₁₉ network with racecar training yields a significantly better output. While these images only provide qualitative information about the properties of racecar training due to the lack of a ground truth result, we have found across a wide range of tests that performing stylization with models from racecar training yields more intuitive and robust results. This is most likely caused by the improved representation these networks form of the input data distribution, which allows them to more clearly separate salient objects and visual styles.

6 Conclusions

We have proposed a novel training approach for improving neural network generalization by adding a constrained reverse pass. We have shown for a wide range of scenarios, from singular value decompositions, over mutual information, to transfer learning benchmarks, that racecar training yields networks with better generalizing capabilities. Our training approach is very general and imposes no requirements regarding network structure or training methods. As future work, we believe it will be very interesting to evaluate our approach in additional contexts, e.g., for temporal structures [22, 6], and for training explainable and interpretable models [55, 5, 10].

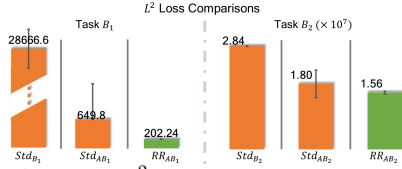


Figure 9: L^2 loss comparisons for two different smoke transfer learning tasks (averaged across 5 runs each). The RR models show the best performance for both tasks.

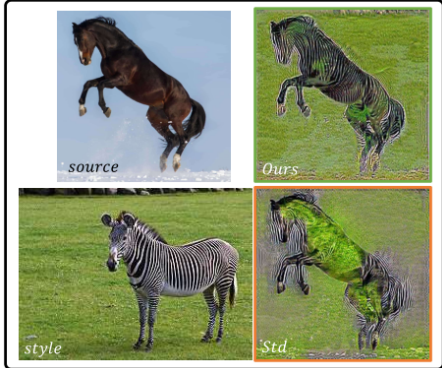


Figure 10: Stylization cases from horse to zebra.

Supplemental Material for *Data-driven Regularization via Racecar Training for Generalizing Neural Networks*

Below, we provide additional details regarding derivation, data sets, network architectures, and experiments mentioned in the main paper. We additionally show results that could not be included in the main document due to page restrictions: an MNIST classification case (Sec. C.1), natural image classification (Sec. C.2), and additional generation and stylization results in Sec. D.2 and Sec. D.4, respectively.

To ensure reproducibility, source code for all tests will be published, in addition to all data sets that are not readily available. The runtimes below were measured on a machine with Nvidia GeForce GTX 1080 Ti GPUs and an Intel Core i7-6850K CPU.

A Method

A.1 Racecar Loss and SVD

In this section we give a more detailed derivation of our racecar loss formulation and extends on the information given in Section 3 of the main paper. As explained there, the racecar loss aims for minimizing

$$\mathcal{L}_{RR} = \sum_{m=1}^n (M_m^T M_m \mathbf{d}_m^i - \mathbf{d}_m^i)^2, \quad (11)$$

where $M_m \in \mathbb{R}^{s_m^{\text{out}} \times s_m^{\text{in}}}$ denotes the weight matrix of layer m , and data from the input data set \mathcal{D}_m is denoted by $\mathbf{d}_m^i \in \mathbb{R}^{s_m^{\text{in}}}$, $i = 1, 2, \dots, t$. Here t denotes the number of samples in the input data set. Minimizing Eq. (11) is mathematically equivalent to

$$M_m^T M_m \mathbf{d}_m^i - \mathbf{d}_m^i = \mathbf{0} \quad (12)$$

for all \mathbf{d}_m^i . Hence, perfectly fulfilling Eq. (11) would require all \mathbf{d}_m^i to be eigenvectors of $M_m^T M_m$ with corresponding eigenvalues being 1. As in Sec. 3 of the main paper, we make use of an auxiliary orthonormal basis $\mathcal{B}_m : \langle \mathbf{w}_m^1, \dots, \mathbf{w}_m^q \rangle$, for which q (with $q \leq t$) denotes the number of linearly independent entries in \mathcal{D}_m . While \mathcal{B}_m never has to be explicitly constructed for our method, it can, e.g., be obtained via Gram-Schmidt. The matrix consisting of the vectors in \mathcal{B}_m is denoted by D_m .

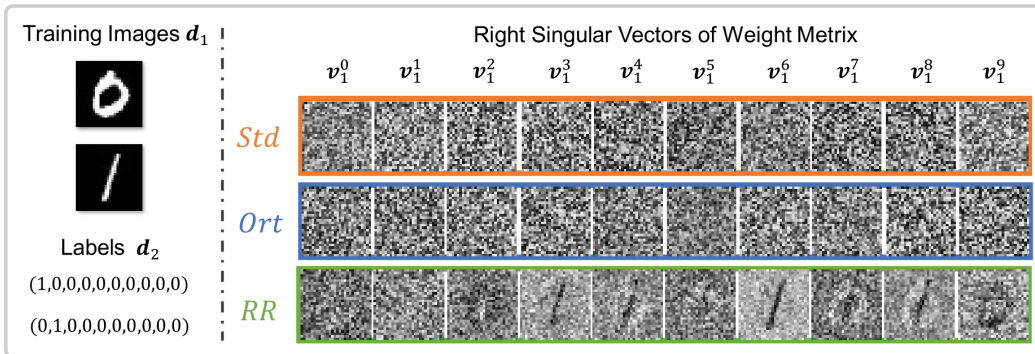


Figure 11: An example of the intuitive analysis of network weights enabled by racecar training: we show the singular vectors for a conventional model **Std**, a model trained with orthogonal constraints **Ort**, and a racecar version **RR**. The singular vectors from racecar training show clear structures that resemble the inputs, while the other variants contain no visible structures. The evaluation via LPIPS of \mathbf{d}_1 versus all \mathbf{v}_1 confirms this: it yields 0.316 for **RR** on average, which is significantly better than **Ort** with 0.504) and **Std** with 0.484. Details and further examples are given in Sec. A.3 below.

Since the $\mathbf{w}_m^h (h = 1, 2, \dots, q)$ necessarily can be expressed as linear combinations of \mathbf{d}_m^i , Eq. (11) similarly requires \mathbf{w}_m^h to be eigenvectors of $M_m^T M_m$ with corresponding eigenvalues being 1, i.e.:

$$M_m^T M_m \mathbf{w}_m^h - \mathbf{w}_m^h = \mathbf{0} \quad (13)$$

We denote the vector of coefficients to express \mathbf{d}_m^i via D_m with \mathbf{c}_m^i , i.e. $\mathbf{d}_m^i = D_m \mathbf{c}_m^i$. Then Eq. (12) can be rewritten as:

$$M_m^T M_m D_m \mathbf{c}_m^i - D_m \mathbf{c}_m^i = \mathbf{0} \quad (14)$$

Via an SVD of the matrix M_m in Eq. (14) we obtain

$$\begin{aligned} & M_m^T M_m D_m \mathbf{c}_m - D_m \mathbf{c}_m \\ &= \sum_{h=1}^q M_m^T M_m \mathbf{w}_m^h \mathbf{c}_{m_h} - \mathbf{w}_m^h \mathbf{c}_{m_h} \\ &= \sum_{h=1}^q V_m \Sigma_m^T \Sigma_m V_m^T \mathbf{w}_m^h \mathbf{c}_{m_h} - \mathbf{w}_m^h \mathbf{c}_{m_h} \end{aligned} \quad (15)$$

where the coefficient vector \mathbf{c}_m is accumulated over the training data set size t via $\mathbf{c}_m = \sum_{i=1}^t \mathbf{c}_m^i$. Here we assume that over the course of a typical training run eventually every single datum in \mathcal{D}_m will contribute to $\mathcal{L}_{\text{RR}_m}$. This form of the loss highlights that minimizing $\mathcal{L}_{\text{RR}_m}$ requires an alignment of $V_m \Sigma_m^T \Sigma_m V_m^T \mathbf{w}_m^h \mathbf{c}_{m_h}$ and $\mathbf{w}_m^h \mathbf{c}_{m_h}$.

By construction, Σ_m contains the square roots of the eigenvalues of $M_m^T M_m$ as its diagonal entries. The matrix has rank $r = \text{rank}(M_m^T M_m)$, and since all eigenvalues are required to be 1 by Eq. (13), the multiplication with Σ_m in Eq. (15) effectively performs a selection of r column vectors from V_m . Hence, we can focus on the interaction between the basis vectors \mathbf{w}_m and the r active column vectors of V_m :

$$\begin{aligned} & V_m \Sigma_m^T \Sigma_m V_m^T \mathbf{w}_m^h \mathbf{c}_{m_h} - \mathbf{w}_m^h \mathbf{c}_{m_h} \\ &= \mathbf{c}_{m_h} (V_m \Sigma_m^T \Sigma_m V_m^T \mathbf{w}_m^h - \mathbf{w}_m^h) \\ &= \mathbf{c}_{m_h} \left(\sum_{f=1}^r (\mathbf{v}_m^f)^T \mathbf{w}_m^h \mathbf{v}_m^f - \mathbf{w}_m^h \right). \end{aligned} \quad (16)$$

As V_m is obtained via an SVD it contains r orthogonal eigenvectors of $M_m^T M_m$. Eq. (13) requires $\mathbf{w}_m^1, \dots, \mathbf{w}_m^q$ to be eigenvectors of $M_m^T M_m$, but since typically the dimension of the input data set is much larger than the dimension of the weight matrix, i.e. $r \leq q$, in practice only r vectors from \mathcal{B}_m can fulfill Eq. (13). This means the vectors $\mathbf{v}_m^1, \dots, \mathbf{v}_m^r$ in V_m are a subset of the orthonormal basis vectors $\mathcal{B}_m : \langle \mathbf{w}_m^1, \dots, \mathbf{w}_m^q \rangle$ with $(\mathbf{w}_m^h)^2 = 1$. Then for any \mathbf{w}_m^h we have

$$\begin{cases} (\mathbf{v}_m^f)^T \mathbf{w}_m^h = 1, & \text{if } \mathbf{v}_m^f = \mathbf{w}_m^h \\ (\mathbf{v}_m^f)^T \mathbf{w}_m^h = 0, & \text{otherwise.} \end{cases} \quad (17)$$

Thus if V_m contains \mathbf{w}_m^h , we have

$$\sum_{f=1}^r (\mathbf{v}_m^f)^T \mathbf{w}_m^h \mathbf{v}_m^f = \mathbf{w}_m^h, \quad (18)$$

and we trivially fulfill the constraint

$$\mathbf{c}_{m_h} \left(\sum_{f=1}^r (\mathbf{v}_m^f)^T \mathbf{w}_m^h \mathbf{v}_m^f - \mathbf{w}_m^h \right) = \mathbf{0}. \quad (19)$$

However, due to r being smaller than q in practice, V_m typically can not include all vectors from \mathcal{B}_m . Thus, if V_m does not contain \mathbf{w}_m^h , we have $(\mathbf{v}_m^f)^T \mathbf{w}_m^h = 0$ for every vector \mathbf{v}_m^f in V_m , which means

$$\sum_{f=1}^r (\mathbf{v}_m^f)^T \mathbf{w}_m^h \mathbf{v}_m^f = \mathbf{0}. \quad (20)$$

As a consequence, the constraint Eq. (12) is only partially fulfilled:

$$\mathbf{c}_{m_h} \left(\sum_{f=1}^r (\mathbf{v}_m^f)^T \mathbf{w}_m^h \mathbf{v}_m^f - \mathbf{w}_m^h \right) = -\mathbf{c}_{m_h} \mathbf{w}_m^h. \quad (21)$$

As the \mathbf{w}_m^h have unit length, the factors \mathbf{c}_m determine the contribution of a datum to the overall loss. A feature \mathbf{w}_m^h that appears multiple times in the input data will have a correspondingly larger factor in \mathbf{c}_m and hence will more strongly contribute to \mathcal{L}_{RR} . The L^2 formulation of Eq. (11) leads to the largest contributors being minimized most strongly, and hence the repeating features of the data, i.e., dominant features, need to be represented in V_m to minimize the racecar loss.

In summary, to minimize \mathcal{L}_{RR} , V_m is driven towards containing r orthogonal vectors \mathbf{w}_m^h which represent the most frequent features of the input data, i.e. the dominant features. It is worth emphasizing that above \mathcal{B}_m is only an auxiliary basis, i.e., the derivation does not depend on any particular choice of \mathcal{B}_m .

A.2 Examples of Network Architectures with Racecar Training

To specify NN architectures, we use the following notation: $C(k, l, q)$, and $D(k, l, q)$ denote convolutional and deconvolutional operations, respectively, while fully connected layers are denoted with $F(l)$, where k, l, q denote kernel size, output channels and stride size, respectively. The bias of a CNN layer is denoted with b . $I/O(z)$ denote *input/output*, their dimensionality is given by z . I_r denotes the input of the reverse pass network. \tanh , relu , lrelu denote hyperbolic tangent, ReLU, and leaky ReLU activation functions (AF), where we typically use a leaky tangent of 0.2 for the negative half-space. UP , MP and BN denote $2 \times$ nearest-neighbor up-sampling, max pooling with 2×2 filters and stride 2, and batch normalization, respectively.

Below we provide additional examples how to realize the racecar loss $\mathcal{L}_{\text{racecar}}$ in a neural network architecture. As explained in the main document, the constraint Eq. (11) is formulated via

$$\mathcal{L}_{\text{racecar}} = \sum_{m=1}^n \lambda_m \left\| \mathbf{d}_m - \mathbf{d}'_m \right\|_F^2, \quad (22)$$

with \mathbf{d}_m , and λ_m denoting the vector of activated intermediate data in layer m from the forward pass, and a scaling factor, respectively. \mathbf{d}'_m denotes the activations of layer m from the reverse pass. E.g., let $L_m()$ denote the operations of a layer m in the forward pass, and $L'_m()$ the corresponding operations for the reverse pass. Then $\mathbf{d}_{m+1} = L_m(\mathbf{d}_m)$, and $\mathbf{d}'_m = L'_m(\mathbf{d}'_{m+1})$.

When Eq. (22) is minimized, we obtain activated intermediate content during the reverse pass that reconstructs the values computed in the forward pass, i.e. $\mathbf{d}'_{m+1} = \mathbf{d}_{m+1}$ holds. Then \mathbf{d}'_m can be reconstructed from the incoming activations from the reverse pass, i.e., \mathbf{d}'_{m+1} , or from the output of layer m , i.e., \mathbf{d}_{m+1} . Using \mathbf{d}'_{m+1} results in a global coupling of input and output throughout all layers, i.e., the *full racecar loss* variant. On the other hand, \mathbf{d}_{m+1} yields a variant that ensures local reversibility of each layer, and yields a very similar performance, as we will demonstrate below. We employ this *layer-wise racecar loss* for networks without a unique, i.e., bijective, connection between two layers. Intuitively, when inputs cannot be reliably reconstructed from outputs.

Full Racecar Training: An illustration of a CNN structure with AF and BN and a full racecar loss is shown in Fig. 12. While the construction of the reverse pass is straight-forward for all standard operations, i.e., fully connected layers, convolutions, pooling, etc., slight adjustments are necessary for AF and BN. It is crucial for our formulation that \mathbf{d}_m and \mathbf{d}'_m contain the same latent space content in terms of range and dimensionality, such that they can be compared in the loss. Hence, we use the BN parameters and the AF of layer $m - 1$ from the forward pass for layer m in the reverse pass. An example is shown in Fig. 15.

To illustrate this setup, we consider an example network employing convolutions with mixed AFs, BN, and MP. Let the network receives a field of 32^2 scalar values as input. From this input, 20, 40, and 60 feature maps are extracted in the first three layers. Besides, the kernel sizes are decreased from 5×5 to 3×3 . To clarify the structure, we use ReLU activation for the first convolution, while the second one uses a hyperbolic tangent, and the third one a sigmoid function. With the notation

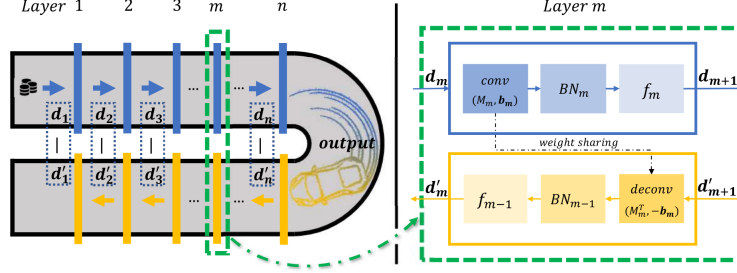


Figure 12: Left: An overview of the regular forward pass (blue) and the corresponding reverse pass (yellow). The right side illustrates how parameters are reused for a convolutional layer. *conv/deconv* denote convolution/deconvolutional operations. f_m and BN_m denote the activation function and batch normalization of layer m , respectively. Shared kernel and bias are represented by M_m and \mathbf{b}_m .

outlined above, the first three layers of the network are

$$\begin{aligned}
 I(32, 32, 1) &= \mathbf{d}_1 \rightarrow C_1(5, 20, 1) + \mathbf{b}_1 \rightarrow BN_1 \rightarrow \text{relu} \\
 &\rightarrow \mathbf{d}_2 \rightarrow MP \rightarrow C_2(4, 40, 1) + \mathbf{b}_2 \rightarrow BN_2 \rightarrow \tanh \\
 &\rightarrow \mathbf{d}_3 \rightarrow MP \rightarrow C_3(3, 60, 1) + \mathbf{b}_3 \rightarrow BN_3 \rightarrow \text{sigm} \\
 &\rightarrow \mathbf{d}_4 \rightarrow \dots
 \end{aligned} \tag{23}$$

The reverse pass for evaluating the racecar loss re-uses all weights of the forward pass and ensures that all intermediate vectors of activations, \mathbf{d}_m and \mathbf{d}'_m , have the same size and content in terms of normalization and non-linearity. We always consider states after activation for $\mathcal{L}_{\text{racecar}}$. Thus, \mathbf{d}_m denotes activations before pooling in the forward pass and \mathbf{d}'_m contains data after up-sampling in the reverse pass, in order to ensure matching dimensionality. Thus, the last three layers of the reverse network for computing $\mathcal{L}_{\text{racecar}}$ take the form:

$$\begin{aligned}
 \dots &\rightarrow \mathbf{d}'_4 \rightarrow -\mathbf{b}_3 \rightarrow D_3(3, 40, 1) \rightarrow BN_2 \rightarrow \tanh \rightarrow UP \\
 &\rightarrow \mathbf{d}'_3 \rightarrow -\mathbf{b}_2 \rightarrow D_2(4, 20, 1) \rightarrow BN_1 \rightarrow \text{relu} \rightarrow UP \\
 &\rightarrow \mathbf{d}'_2 \rightarrow -\mathbf{b}_1 \rightarrow D_1(5, 3, 1) \\
 &\rightarrow \mathbf{d}'_1 = O(32, 32, 1).
 \end{aligned} \tag{24}$$

Here, the de-convolutions D_x in the reverse network share weights with C_x in the forward network. I.e., the $4 \times 4 \times 20 \times 40$ weight matrix of C_2 is reused in its transposed form as a $4 \times 4 \times 40 \times 20$ matrix in D_2 . Additionally, it becomes apparent that AF and BN of layer 3 from the forward pass do not appear in the listing of the three last layers of the reverse pass. This is caused by the fact that both are required to establish the latent space of the fourth layer. Instead, \mathbf{d}_3 in our example represents the activations after the second layer (with BN_2 and \tanh), and hence the reverse pass for \mathbf{d}'_3 reuses both functions. This ensures that \mathbf{d}_m and \mathbf{d}'_m contain the same latent space content in terms of range and dimensionality, and can be compared in Eq. (22).

For the reverse pass, we additionally found it beneficial to employ an AF for the very last layer if the output space has suitable content. E.g., for inputs in the form of RGB data we employ an additional activation with a ReLU function for the output to ensure the network generates only positive values. The architectures in Tab. 11, 13, 15, 19, 22, and 24 use such an activation.

Layer-wise Racecar Training: In the example above, we use a full racecar training with \mathbf{d}'_{m+1} to reconstruct the activations \mathbf{d}'_m . The full racecar structure establishes a slightly stronger relationship among the racecar loss terms of different layers, and allows earlier layers to decrease the accumulated loss of later layers. However, if the architecture of the original network makes use of operations between layers that are not bijective, we instead use the layer-wise racecar loss. E.g., this happens for residual connections with an addition or non-invertible pooling operations such as max-pooling. In the former, we cannot uniquely determine the b, c in $a = b + c$ given only a . And unless special care is taken [4], the source neuron of an output is not known for regular max-pooling operations. Note that our racecar loss has no problems with irreversible operations within a layer, e.g., most convolutional or fully-connected layers typically are not fully invertible. In all these cases the loss will drive the network towards a state that is as-invertible-as-possible for the given input data set. However, this requires a reliable vector of target activations in order to apply the constraints. If the

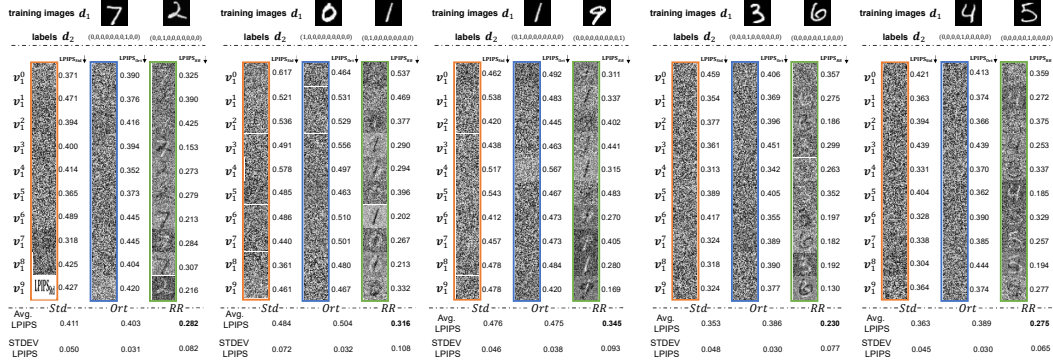


Figure 13: SVD of the M_1 matrix for five tests with random two digit images as training data. LPIPS distances [57] of **RR** are consistently lower than **Std** and **Ort**.

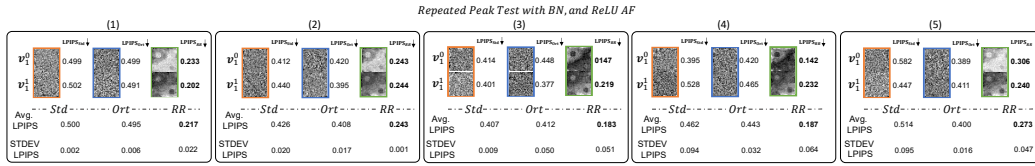


Figure 14: Five repeated tests with the peak data shown in Sec. 3 of the main paper. **RR_A** robustly extracts dominant features from the data set. The two singular vectors strongly resemble the two peak modes of the training data. This is confirmed by the LPIPS measurements.

connection between layers is not bijective, we cannot reconstruct this target for the constraints, as in the examples given above.

In such cases, we regard every layer as an individual unit to which we apply the racecar loss by building a layer-wise reverse pass. For example, given a simple convolutional architecture with

$$\mathbf{d}_1 \rightarrow C_1(5, 20, 1) + \mathbf{b}_1 = \mathbf{d}_2 \quad (25)$$

in the forward pass, we calculate \mathbf{d}'_1 with

$$(\mathbf{d}_2 - \mathbf{b}_1) \rightarrow D_1(5, 3, 1) = \mathbf{d}'_1, \quad (26)$$

We, e.g., use this layer-wise loss in the Resnet10 network shown in Tab. 17.

A.3 MNIST and Peak tests

Below we give details for the MNIST and *peak* tests from Sec. 3 of the main paper.

MNIST Test : For the MNIST test, additional SVDs of the weight matrices of trained models can be seen in Fig. 11 and Fig. 13. The LPIPS scores (lower being better) show that features embedded in the weights of **RR** are significantly closer to the training data set than **Std** and **Ort**. All MNIST models are trained for 1000 epochs with a learning rate of 0.0001, and $\lambda = 1e - 5$ for **RR_A**. The NN architecture of the tests in this section is given in Tab. 8.

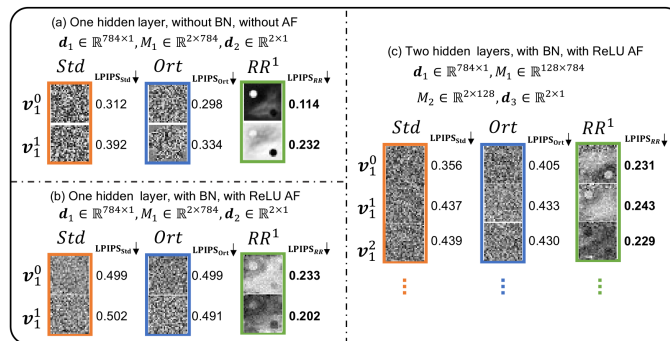


Figure 15: Right singular vectors of M_1 for peak tests with different network architectures: from a single linear layer to two layers with BN and AF. Across the three architectures, **RR_A** successfully extracts dominant features. In contrast to **Std** and **Ort**, the singular vectors contain salient structures.

Peak Test : For the *Peak* test we generated a data set of 110 images shown in Fig. 16. 55 images contain a peak located in the upper left corner of the image. The other 55 contain a peak located in the bottom right corner. We added random scribbles in the images to complicate the task. All 110 images were labeled with a one-hot encoding of the two possible positions of the peak. We use 100 images as training data set, and the remaining 10 for testing. All peak models are trained for 5000 epochs with a learning rate of 0.0001, with $\lambda = 1e - 6$ for RR_A . To draw reliable conclusions, we show results for five repeated runs here. The neural network in this case contains one fully connected layer, with BN and ReLU activation. The results are shown in Fig. 14, with both peak modes being consistently embedded into the weight matrix of RR_A , while regular and orthogonal training show primarily random singular vectors.

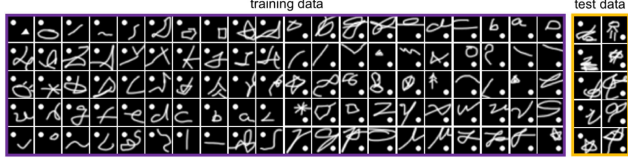


Figure 16: Data set used for the *peak* tests.

We also use different network architectures in Fig. 15 to verify that the dominant features are successfully extracted when using more complex network structures. Even for two layers with BN and ReLU activations, the racecar training clearly extracts the two modes of the training data. The visual resemblance is slightly reduced in this case, as the network has the freedom to embed the features in both layers. Across all three cases (for which we performed 5 runs each), the racecar training clearly outperforms regular training and the orthogonality constraint in terms of extracting and embedding the dominant structures of the training data set in the weight matrix.

Overall, our experiments confirm the theory behind the racecar formulation. They additionally show that racecar training in combination with a subsequent SVD of the network weights yields a simple and convenient method to give humans intuition about the features learned by a network.

B Evaluation via Mutual Information

This section gives details of the mutual information and disentangled representation tests from Sec. 4 of the main paper.

B.1 Mutual Information test

We now evaluate our approach in terms of mutual information (MI), which measures the dependence of two random variables, i.e., higher MI means that there is more shared information between two parameters. More formally, the mutual information $I(X; Y)$ of random variables X and Y measures how different the joint distribution of X and Y is w.r.t. the product of their marginal distributions, i.e., the Kullback-Leibler divergence $I(X; Y) = \text{KL}[P_{(X,Y)} || P_X P_Y]$, where KL denotes the Kullback-Leibler divergence. Let $I(X; \mathcal{D}_m)$ denote the mutual information between the activations of a layer \mathcal{D}_m and input X . Similarly $I(\mathcal{D}_m; Y)$ denotes the MI between layer m and the output Y . We use *MI planes* in the main paper, which show $I(X; \mathcal{D}_m)$ and $I(\mathcal{D}_m; Y)$ in a 2D graph for the activations of each layer \mathcal{D}_m of a network after training. This visualizes how much information about input and output distribution is retained at each layer, and how these relationships change within the network. For regular training, the information bottleneck principle [48] states that early layers contain more information about the input, i.e., show high values for $I(X; \mathcal{D}_m)$ and $I(\mathcal{D}_m; Y)$. Hence in the MI plane visualizations, these layers are often visible at the top-right corner. Later layers typically share a large amount of information with the output after training, i.e. show large $I(\mathcal{D}_m; Y)$ values, and correlate less with the input (low $I(X; \mathcal{D}_m)$). Thus, they typically show up in the top-left corner of the MI plane graphs.

Training Details: We use the same numerical studies as in [42] as task A , i.e. a regular feed-forward neural network with 6 fully-connected layers. The input variable X contains 12 binary digits that represent 12 uniformly distributed points on a 2D sphere. The learning objective is to discover binary decision rules which are invariant under $O(3)$ rotations of the sphere. X has 4096 different patterns, which are divided into 64 disjoint orbits of the rotation group, forming a minimal sufficient partition for spherically symmetric rules [27]. To generate the input-output distribution $P(X, Y)$, We apply the stochastic rule $p(y = 1|x) = \Psi(f(x) - \theta)$, ($x \in X, y \in Y$), where Ψ is a standard sigmoidal

function $\Psi(u) = 1/(1 + \exp(-\gamma u))$, following [42]. We then use a spherically symmetric real valued function of the pattern $f(x)$, evaluated through its spherical harmonics power spectrum [27], and compare with a threshold θ , which was selected to make $p(y = 1) = \sum_x p(y = 1|x)p(x) \approx 0.5$, with uniform $p(x)$. γ is high enough to keep the mutual information $I(X; Y) \approx 0.99$ bits.

For the transfer learning task B , we reverse output labels to check whether the model learned specific or generalizing features. E.g., if the output is $[0,1]$ in the original data set, we swap the entries to $[1,0]$. 80% of the data (3277 data pairs) are used for training and rests (819 data pairs) are used for testing. The forward and reverse pass architectures of the fully connected neural networks are given in Tab. 9. Hyperparameters used for training are listed in Tab. 10. Models are trained using cross-entropy as the base loss function.

For the MI comparison in Fig. 4 of the main paper, we discuss models before and after fine-tuning separately, in order to illustrate the effects of regularization. We include a regular model Std_A , one with orthogonality constraints Ort_A , and our regular racecar model RR_A , all before fine-tuning. For the regular racecar model RR_A all layers are constrained to be recovered in the backward pass. We additionally include the version RR_A^1 , i.e. a model trained with only one racecar loss term $\lambda_1 |d_1 - d'_1|_2$, which means that only the input is constrained to be recovered. Thus, RR_A^1 represents a simplified version of our approach which receives no constraints that intermediate results of the forward and backward pass should match. For Ort_A , we used the Spectral Restricted Isometry Property (SRIP) regularization [2],

$$\mathcal{L}_{\text{SRIP}} = \beta \sigma(W^T W - I), \quad (27)$$

where W is the kernel, I denotes an identity matrix, and β represents the regularization coefficient. $\sigma(W) = \sup_{z \in \mathbb{R}^n, z \neq 0} \frac{\|Wz\|}{\|z\|}$ denotes the spectral norm of W .

As explained in the main text, all layers of the first stage, i.e. from RR_A , RR_A^1 , Ort_A and Std_A are reused for training the fine-tuned models without regularization, i.e. RR_{AA} , RR_{AA}^1 , Ort_{AA} and Std_{AA} . Likewise, all layers of the transfer task models RR_{AB} , RR_{AB}^1 , Ort_{AB} and Std_{AB} are initialized from the models of the first training stage.

Analysis of Results: We first compare the version only constraining input and output reconstruction (RR_A^1) and the full racecar loss version RR_A . Fig. 4(b) of the main paper shows that all points of RR_A are located in a central region of the MI plane, which means that all layers successfully encode information about the inputs as well as the outputs. This also indicates that every layer contains a similar amount of information about X and Y , and that the path from input to output is similar to the path from output to input. The points of RR_A^1 , on the other hand, form a diagonal line. I.e., this network has different amounts of mutual information across its layers, and potentially a very different path for each direction. This difference in behavior is caused by the difference of the constraints in these two versions: RR_A^1 is only constrained to be able to regenerate its input, while the full racecar loss for RR_A ensures that the network learns features which are beneficial for both directions. This test highlights the importance of the constraints throughout the depth of a network in our formulation. In contrast, the $I(X; \mathcal{D})$ values of later layers for Std_A and Ort_A exhibit small values (points near the left side), while $I(\mathcal{D}; Y)$ is high throughout. This indicates that the outputs were successfully encoded and that increasing amounts of information about the inputs are discarded. Hence, more specific features about the given output data-set are learned by Std_A and Ort_A . This shows that both models are highly specialized for the given task, and potentially perform worse when applied to new tasks.

During the fine-tuning phase for task A (i.e. regularizers being disabled), all models focus on the output and maximize $I(\mathcal{D}; Y)$. There are differences in the distributions of the points along the y-axis, i.e., how much MI with the output is retained, as shown in Fig. 4(c) of the main paper. For model RR_{AA} , the $I(\mathcal{D}; Y)$ value is higher than for Std_{AA} , Ort_{AA} and RR_{AA}^1 , which means outputs of RR_{AA} are more closely related to the outputs, i.e., the ground truth labels for task A . Thus, RR_{AA} outperforms the other variants for the original task.

In the fine-tuning phase for task B , Std_{AB} stands out with very low accuracy in Fig. 5 of the main paper. This model from a regular training run has large difficulties to adapt to the new task. Model Ort_{AB} also performs worse than Std_B . RR_{AB} shows the best performance in this setting, demonstrating that our loss formulation helped to learn more generic features from the input data. This improves the performance for related tasks such as the inverted outputs used for B .

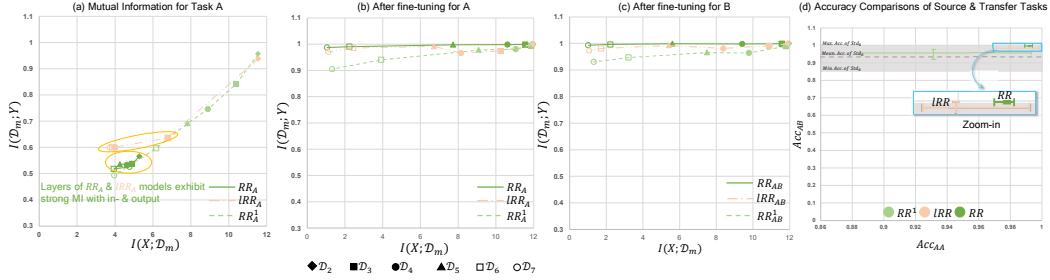


Figure 17: (a-c) MI plane comparisons for layer-wise (IRR_A) versus full models (RR_A). Points on each line correspond to layers of one type of model. a) MI Plane for task A. All points of RR_A and the majority of points for IRR_A (five out of seven) are located in the center of the graph, i.e., successfully connect in- and output distributions. b,c): After fine-tuning for A/B. The last layer \mathcal{D}_7 of RR_{AA} builds the strongest relationship with Y . $I(\mathcal{D}_7; Y)$ of IRR_A is only slightly lower than RR_{AA} . d): Accuracy comparisons among different models: RR_{AA} yields the highest performance, while IRR_A performs similarly with RR_{AA} .

We also analyze the two variants of racecar training, the layer-wise variant IRR_A and the full version RR_A in terms of mutual information. Fig. 17 shows the MI planes for these two models, also showing RR_A^1 for comparison. Despite the local nature of IRR_A it manages to establish MI for the majority of the layers, as indicated by the cluster of layers in the center of the MI plane. Only the first layer moves towards the top right corner, and the second layer is affected slightly. I.e., these layers exhibit a stronger relationship with the distribution of the outputs. Despite this, the overall performance when fine-tuning or for the task transfer remains largely unaffected, e.g., the IRR_A still clearly outperforms RR_A^1 . This confirms our choice to use the full racecar training when network connectivity permits, and employ the layer-wise version in all other cases.

Numerical accuracies for all models discussed in this section are listed in Tab. 1 and Tab. 2. Mutual information values, i.e., $I(X, \mathcal{D}_m)$ and $I(\mathcal{D}_m, Y)$, for all models and layers are provided in Tab. 26.

B.2 Disentangled Representations

The InfoGAN approach [5] demonstrated the possibility to control the output of generative models via maximizing mutual information between outputs and structured latent variables. However, mutual information is very hard to estimate in practice [51]. The previous section and Fig. 4(b) of the main paper demonstrated that models from racecar training (both RR_A^1 and RR_A) can increase the mutual information between network inputs and outputs. Intuitively, racecar training explicitly constrains the model to recover an input given an output, which directly translates into an increase of mutual information between input and output distributions compared to regular training runs. For highlighting how racecar training can yield disentangled representations (as discussed in the later paragraphs of Sec. 4 of the main text), we follow the experimental setup of InfoGAN [5]: the input dimension of our network is 74, containing 1 ten-dimensional category code c_1 , 2 continuous latent codes $c_2, c_3 \sim \mathcal{U}(-1, 1)$ and 62 noise variables. Here, \mathcal{U} denotes a uniform distribution.

Training Details: As InfoGAN focuses on structuring latent variables and thus only increases the mutual information between latent variables and the output, we also focus the racecar training on the corresponding latent variables. I.e., the goal is to maximize their mutual information with the output of the generative model. Hence, we train a model RR^1 for which only latent dimensions c_1, c_2, c_3 of the input layer are involved in the racecar loss. We still employ a full reverse pass structure in the neural network architecture. c_1 is a ten-dimensional category code, which is used for controlling the output digit category, while c_2 and c_3 are continuous latent codes, to represent (previously unknown) key properties of the digits, such as orientation or thickness. Building relationship between c_1 and outputs is more difficult than for c_2 or c_3 , since the 10 different digit outputs need to be encoded in a single continuous variable c_1 . Thus, for the corresponding racecar loss term for c_1 we use a slightly larger λ factor (by 33%) than for c_2 and c_3 . The forward and reverse pass architectures of the network are given in Tab. 11, and hyperparameters are listed in Tab. 12. Details of our results are shown in Fig. 18. Models are trained using a GAN loss [17] as the loss function for the outputs.

Analysis of Results : In Fig. 18 we show additional results for the disentangling test case. It is visible that the racecar training with the RR^1 model yield distinct and meaningful latent space

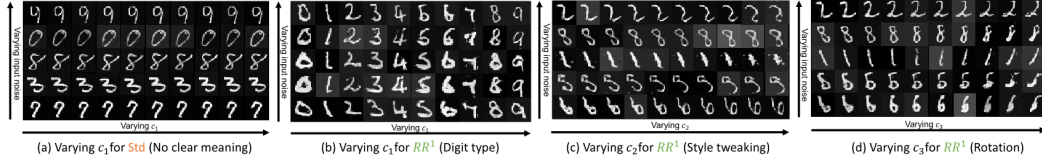


Figure 18: Additional results for the disentangled representations with the MNIST data: For every row in the figures, we vary the corresponding latent code (left to right), while keeping all other inputs constant. Different rows indicate a different random noise input. For example, in (b): every column contains five results which are generated with different noise samples, but the same latent codes $c_{1\sim 3}$. In every row, 10 results are generated with 10 different values of c_1 , which correspond to one digit each for (b). (a): For a regular training (**Std**), no clear correspondence between c_1 and the outputs are apparent (similarly for $c_{2,3}$). (c): Different c_2 values result in a tweaked style, while c_3 controls the orientation of the digit, as shown in (d). Thus, in contrast to **Std**, the racecar model learns a meaningful, disentangled representation.

dimensions for $c_{1,2,3}$. While c_1 controls the digit, $c_{2,3}$ control the style and orientation of the digits. For comparison, a regular training run with model **Std** does result in meaningful or visible changes when adjusting the latent space dimensions. This illustrates how strongly racecar training can shape the latent space, and in addition to an intuitive embedding of dominant features, yield a disentangled representation.

C Additional Experiments

In this section we present several additional experiments that were not included in the main document due to space constraints.

C.1 MNIST Classification

The MNIST data set is a commonly used data set for hand written digit classification [32]. We train three types of models with the regular MNIST data set: one with racecar loss **RR**, a regular model **Std**, and one with orthogonal constraints **Ort** [2] for comparison. Usually, convolutional layers take up most of the model parameters, so we correspondingly compute the racecar loss for the convolutional layers, omitting the fully connected layers that would be required for class label inference. We follow the common practice to first train models with regularization and then fine-tune without [2]. As we discuss model states before fine-tuning in this section, we use the following naming scheme with suffixes *zni*, *MNI* and *n-MNI* to distinguish the different phases. E.g., with racecar training: **RR_{zni}** for training runs on MNIST with regularization, **RR_{MNI}** for fine-tuning on MNIST without regularization using **RR_{zni}** as starting point, and **RR_{n-MNI}** for fine-tuning on a transfer task without regularization, likewise using **RR_{zni}** as starting point.

Training Details: The regular MNIST data set [32] contains $55k$ images for training and $10k$ images for testing. For the n-MNIST motion blur data set [3], there are $60k$ images for training and $10k$ images for testing. All images have a size of 28×28 . Example data from n-MNIST that illustrates the motion blur is shown in Fig. 20. Details of the network architectures are shown in Tab. 15, with hyperparameters given in Tab. 16. The models are trained using cross-entropy as base loss function, and all three convolutional layers are used for the racecar loss.

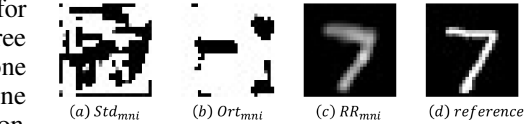


Figure 19: Comparisons between reconstructed inputs. Only **RR_{zni}** recovers most of the input information successfully.

Analysis of Results : To highlight the properties of our algorithm, we show comparisons between the original input d_1 and the reconstructed inputs d'_1 in Fig. 19 for the models **RR_{zni}**, **Std_{zni}**, and **Ort_{zni}**. These models were trained with an enabelde regularization, i.e., before fine tuning. For



Figure 20: Example data from n-MNIST.

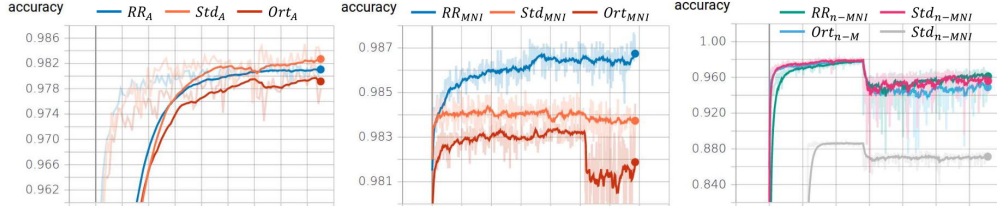


Figure 22: Visualizations of training processes for the MNIST cases. Left, constraints enabled: RR_{mni} (accuracy: 0.9810, perf.: 5.675 s/epoch), Std_{mni} (accuracy: 0.9827, perf.: 3.522 s/epoch) and Ort_{mni} (accuracy: 0.9792, perf.: 4.969 s/epoch). Middle, fine tuning: RR_{MNI} , Std_{MNI} and Ort_{MNI} . Right, task transfer: RR_{n-MNI} , Std_{n-MNI} , Ort_{n-MNI} , and Std_B .

racecar training, most of the features from the input are recovered, while trying to invert the network in the same way for a regular training run or a training with orthogonal constraints largely fails. In both cases, features are extracted only according to the digit classification task, and both models discard information unrelated to this goal.

For the final MNIST models including fine-tuning, i.e., Ort_{MNI} , Std_{MNI} , and RR_{MNI} , results are shown in Fig. 21 for 5 repeated runs. We can see that RR_{MNI} outperforms Ort_{MNI} and Std_{MNI} , which indicates that racecar training yields generic features that can also improve performance for the original task.

As generic features are typically more robust than specific features [36], we investigate a perturbed data set with motion blur (n-MNIST [3]) for the task transfer. We fine-tune all three previous models for the n-MNIST data set, to obtain the models Ort_{n-MNI} , Std_{n-MNI} , and RR_{n-MNI} . Performance results are likewise given in Fig. 21. Based on the same CNN architecture and parameters, RR_{mni} achieves the best performance. This indicates that the RR model learned more generic features via racecar training than Ort and Std . Interestingly, the racecar training not only improves inference accuracy, but also stabilizes training, as indicated by the variance of the results in Fig. 21.

For fine-tuning the models without regularization, i.e. for training RR_{MNI}/RR_{n-MNI} , Std_{MNI}/Std_{n-MNI} and Ort_{MNI}/Ort_{n-MNI} , we load RR_{mni} , Std_{mni} , and Ort_{mni} , and continue training without any orthogonalization or racecar loss terms. Example training processes of the MNIST tests are shown in Fig. 22. We can see that the racecar loss increases the task difficulty, so RR_{mni} exhibits a slightly lower performance and longer training time than Std_{mni} in the first phase. In the second phase RR_{mni} outperforms Std_{mni} and Ort_{mni} for both tasks. This illustrates that the dominant features extracted by racecar training also improved performance for both task domains. Numeric accuracies of all models are given in Tab. 3 and Tab. 4.

C.2 Natural Image Classification

Natural images arise in many important application scenarios, and in Sec.5 of the main paper we evaluated racecar training for a very deep ResNet110 for CIFAR 10 [28]. This experiment already demonstrated that racecar training can yield substantial gains in SOTA performance compared to orthogonality constraints. These gains are on a level that is similar with gains that orthogonality constraints exhibit over a regular training. Details of the corresponding Resnet110 accuracies, network architecture, and hyperparameters are shown in Tab. 7, 17 and 18, respectively. To show that racecar training also yields gains in shallow networks, we additionally evaluate our approach with the CIFAR data set using a 19-layer network.

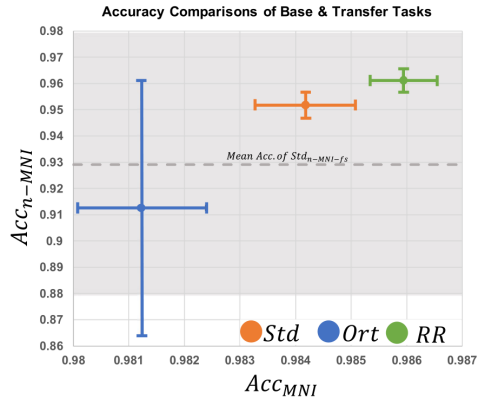


Figure 21: Accuracy comparisons for original task (Acc_{MNI}) and transfer learning task (Acc_{n-MNI}). The dashed grey line and grey region represent the accuracy of baseline models, $Std_{n-MNI-fs}$ trained from scratch for n-MNIST. RR_{MNI} and RR_{n-MNI} outperform this baseline, and achieve the best performance for the source task and transfer learning task, respectively.

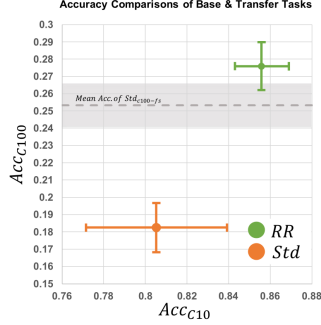


Figure 23: Accuracy comparisons of natural image tasks A and B . Grey line and grey region represent accuracy of baseline $Std_{C100-fs}$. RR_{C10} and RR_{C100} got best performance for task A and B .

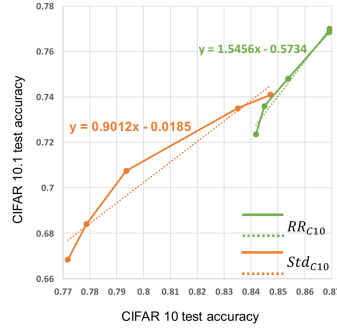


Figure 24: Accuracy comparisons when applying models trained on CIFAR 10 to CIFAR 10.1 data.

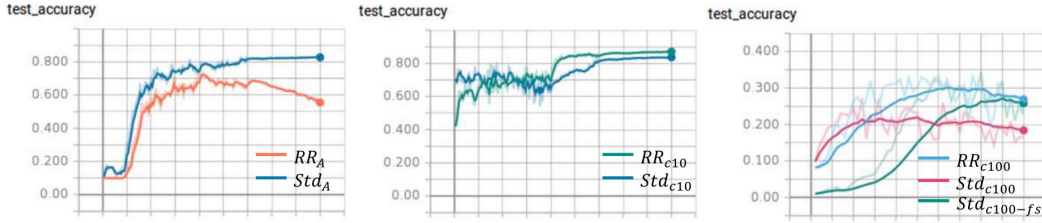


Figure 25: Visualizations of training processes. Left: CIFAR 10 with constraints, RR_{C1} (accuracy: 0.5784, cost: 64 seconds/epoch) and Std_{C1} (accuracy: 0.8272, cost: 63 seconds/epoch). Middle: CIFAR 10, fine tuning, RR_{C10} and Std_{C10} . Right: Task transfer for CIFAR 100, RR_{C100} , Std_{C100} and $Std_{C100-fs}$.

Training Details: Both CIFAR 10 and CIFAR 100 data sets consist of $60k$ 32×32 images. $50k$ of them are used for training and $10k$ of them are used for testing. classes. The forward and reverse pass architectures of the network can be found in Tab. 19 with parameters given in Tab. 20. Models are trained using cross-entropy as loss function, and all 13 convolutional layers are used for the racecar loss. For fine-tuning on CIFAR 100, the last layer is omitted when loading due to the changed size of the output.

Analysis of Results: At first, we train two models with the CIFAR 10 data set as classification task $C10$, i.e., RR_{C1} and Std_{C1} . Example training processes of the CIFAR tests are shown in Fig. 25. We fine-tune to obtain RR_{C10} and Std_{C10} , results for which are shown in Fig. 23. Numerical results are given in Tab. 5. The racecar training also improves performance for this natural image classification task. As transfer learning task we fine-tune RR_{C1} and Std_{C1} for the CIFAR 100 data set classification, yielding models RR_{C100} and Std_{C100} . Results are likewise shown in Fig. 23. Training with the same CNN architecture and parameters, Std_{C1} has difficulties adjusting to the new task, while our model from the initial racecar training even slightly outperforms a model trained from scratch for CIFAR 100 ($Std_{C100-fs}$).

As in the main text, we evaluate these models with the CIFAR transfer benchmark from Recht et al. [41]. It measures how well models trained on the original CIFAR data set, i.e. CIFAR 10, generalize to a new data set (CIFAR 10.1) collected according to the same principles as the original CIFAR 10. Here, it is additionally interesting to see how well performance for CIFAR 10 translates into transfer performance for 10.1. As shown in Fig. 24, estimating the slope of this relationship with a linear fit yields 0.9012 for Std_{C10} , and 1.5456 for RR_{C10} . Thus, while regular training performs worse on the new data when its performance for the original task increases (with a slope of less than one), the models from racecar training very successfully translate gains in performance from the original task to the new one. This indicates that the models have successfully learned a set of generalizing features.

D Experimental Results

Below, we give additional details for the experiments of Sec. 5 of the main paper.

D.1 Texture-shape Benchmark

Training Details: All training data of the texture-shape tests were obtained from [15]. The stylized data set contains 1280 images, 1120 images are used as training data, and 160 as test data. Both edge and filled data sets contain 160 images each, all of which are used for testing only. All three sets (stylized, edge, and filled) contain data for 16 different classes. The forward and reverse pass architectures of the network are given in Tab. 13, with hyperparameters in Tab. 14. Numerical accuracy for RR_{TS} , Ort_{TS} and Std_{TS} is given in Tab. 27, Tab. 28 and Tab. 29, respectively.

Analysis of Results : For a detailed comparison, we list per-class accuracy of stylized data training runs for Ort_{TS} , Std_{TS} and RR_{TS} in Fig. 26. RR_{TS} outperforms the other two models for most of the classes. Training times (in seconds) for different models are listed in Tab. 30. RR_{TS} requires 41.86% more time for training compared to Std_{TS} , but yields a 23.76% higher performance. All models saturated, i.e. training Std_{TS} or Ort_{TS} longer does not increase classification accuracy any further. We also investigated how much we can reduce model size when using racecar training in comparison to the baselines. A reduced racecar model only has 67.94% of the parameters, while still outperforming Ort_{TS} .

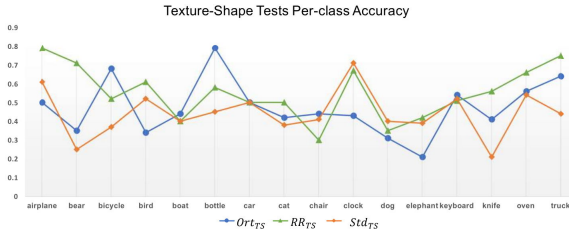


Figure 26: Test accuracy for all 16 classes for the three model variants.

D.2 Generative Adversarial Models

Training Details: The data set of smoke simulation was generated with a fluid solver from an open-source library [47]. We generated 20 simulations with 120 frames each, with 10% of the data being used for training. Smoke inflow region, inflow velocity, and buoyancy force were randomized to produce varied data. The low-resolution data were down-sampled from the high-resolution data by a factor of 4. Data augmentation, such as flipping and rotation was used in addition. As outlined in the main text, we consider building an autoencoder model for the synthetic data as task B_1 , and a generating samples from a real-world smoke data set as task B_2 . The smoke capture data set for B_2 contains 2500 smoke images from the ScalarFlow data set [12], and we again used 10% of these images as training data set.

Task A : We use a fully convolutional CNN-based architecture for generator and discriminator networks (cf. Tab. 21, and parameters in Tab. 23.). Note that the inputs of the discriminator contain high resolution data (64, 64, 1), as well as low resolution (16, 16, 1), which is up-sampled to (64, 64, 1) and concatenated with the high resolution data. In line with previous work [53], RR_A and Std_A are trained with a non-saturating GAN loss, feature space loss and L2 loss as base loss function. All generator layers are involved in the racecar loss.

Task B_1 : All encoder layers are initialized from RR_A and Std_A when training RR_{AB_1} and Std_{AB_1} . It is worth noting that the reverse pass of the generator is also constrained when training RR_A . So both encoder and decoder are initialized with parameters from RR_A when training RR_{AB_1} . This is not possible for a regular network like Std_{AB_1} , as the weights obtained with a normal training run are not suitable to be transposed. Hence, the de-convolutions of Std_{AB_1} are initialized randomly.

Task B_2 : As the data set for the task B_2 is substantially different and contains RGB images (instead of single channel gray-scale images), we choose the following setups for the RR_A and Std_A models: parameters from all six layers of Std_A and RR_A are reused for initializing decoder part of Std_{AB_2} and RR_{AB_2} . Specially, when initializing the last layer of of Std_{AB_2} and RR_{AB_2} , we copy and stack the parameters from the last layer of Std_A and RR_A into three channels to fit output data size in task B_2 . Here, the encoder part of RR_{AB_2} is not initialized with RR_A , due to the significant gap between training data sets of task B_1 and task B_2 . Our experiments show that only initializing the

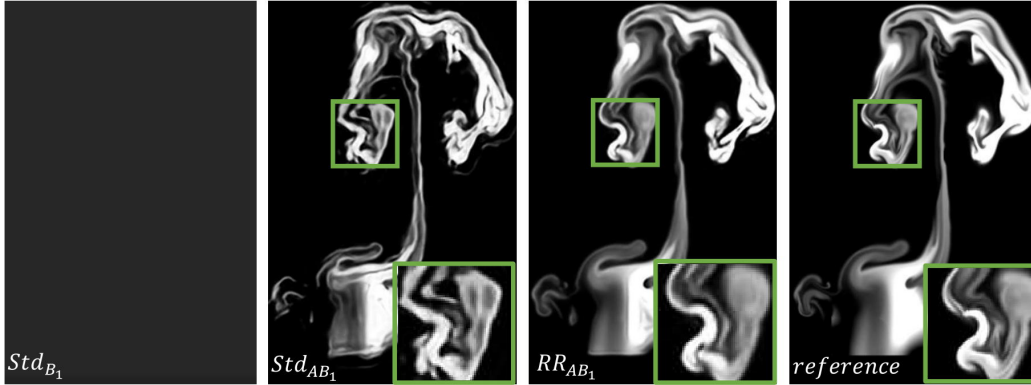


Figure 27: Example outputs for RR_{AB_1} , Std_{AB_1} , Std_{B_1} . The reference is shown for comparison. RR_{AB_1} produces higher quality results than Std_{AB_1} , while a model trained from scratch, Std_{B_1} fails for this task. It produces a mostly black image.

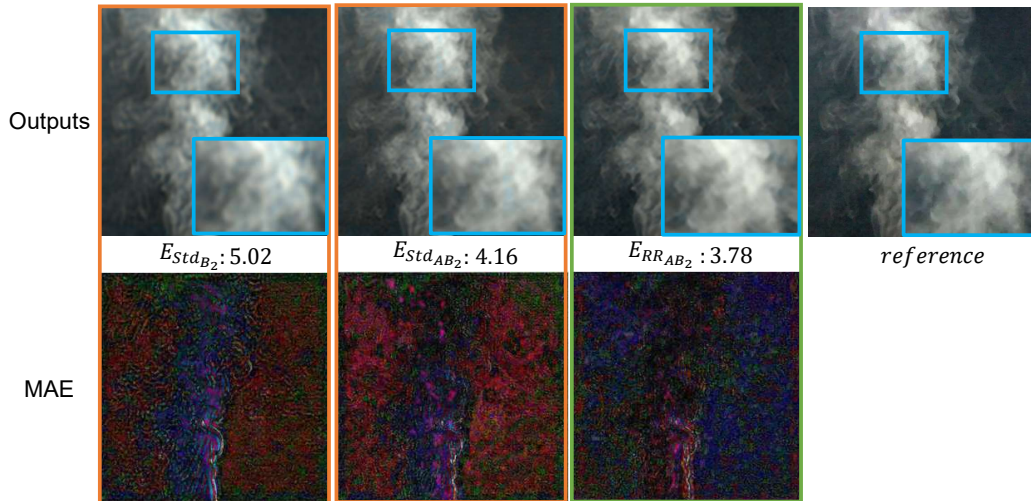


Figure 28: Mean Absolute Error (MAE) comparisons for smoke task B_2 models. RR_{AB_2} shows the smallest error, and additionally achieves the best visual quality amongst the different models. It even outperforms the baseline model trained from scratch, i.e. Std_{B_2} .

decoder part of RR_{AB_2} (avg. loss: $1.56e7$, std. dev.: $3.81e5$) outperforms initializing both encoder and decoder (avg. loss: $1.82e7$, std. dev.: $2.07e6$). We believe the reason is that initializing both encoder and decoder part makes it more difficult to adjust the parameters for new data set that is very different from the data set of the source task.

Analysis of Results: We first discuss the autoencoder transfer learning task AB_1 for synthetic, i.e., simulated fluid data. (architectures for B_1 and B_2 are given in Tab. 22). Example outputs of RR_{AB_1} , Std_{AB_1} and Std_{B_1} are shown in Fig. 27. It is clear that RR_{AB_1} gives the best performance among these models. We similarly illustrate the behavior of the transfer learning task AB_2 for images of real-world fluids. This example likewise uses an autoencoder structure. Visual comparisons are provided in Fig. 28, where RR_{AB_2} generates results that are closer to the reference. Overall, these results demonstrate the benefits of racecar training for GANs, and indicate its potential to obtain more generic features from synthetic data sets that can be used for tasks involving real-world data.

D.3 VGG19 Stylization

The section below gives details of the stylization tests in Sec. 5.4 of the main paper.

VGG19 Training: For the ImageNet data set [7], 1281167 images of 1000 classes are used for training, and 50k images are used for testing. The size of all images is 224×224 . The forward and reverse pass of VGG19 are given in Tab. 24, with hyperparameters shown in Tab. 25. All 16 convolutional layers are used for the racecar loss. To speed up the training process of **RR**, we first train a model without racecar loss for 6 epochs with batch size 64. We then reuse this model for training **RR** and **Std** with a batch size of 24 for 30 epochs.

Stylization Background: Gatys et al. [14] propose to use a loss consisting of a content and a style term, i.e. $\mathcal{L}_{\text{total}} = \eta\mathcal{L}_{\text{content}} + \delta\mathcal{L}_{\text{style}}$, where η and δ denote coefficients. $\mathcal{L}_{\text{content}}$ calculates a content difference between source image p and generated image g :

$$\mathcal{L}_{\text{content}}(p, g, t) = \frac{1}{2} \sum_{m,n} (F_p^{m,n,t} - F_g^{m,n,t})^2, \quad (28)$$

where $F_p^{m,n,t}$ is the feature representation of p of the m^{th} filter at position n in layer t . $\mathcal{L}_{\text{style}}$ instead computes a style difference between style image a and a generated image g :

$$\begin{aligned} G_a^{m,n,t} &= \sum_f F_a^{m,f,t} F_a^{n,f,t}, \\ E_t &= \frac{1}{4N_t^2 M_t^2} \sum_{m,n} (G_g^{m,n,t} - G_a^{m,n,t})^2, \\ \mathcal{L}_{\text{style}}(a, g) &= \sum_{t=0}^T \omega_t E_t, \end{aligned} \quad (29)$$

where ω_t is the weighting factors for layer t ; G is the Gram matrix; N_t denotes filter numbers of layer t , and M_t is the dimension of layer t 's filter. T denotes the number of layers included in the style loss.

D.4 Additional Stylization Results

To compare the feature extracting capabilities between the **RR** and **Std** runs, we only optimize $\mathcal{L}_{\text{style}}$ as a first test. Two geometric shapes are given as source and style images, as shown in Fig. 29. They have the same background and object color. The only difference is the large-scale shape of the object. Thus, as we aim for applying a style that is identical to the source, we can test whether the features can clearly separate and preserve the large scale shape features from the ones for the localized style. Comparing the results of **RR** and **Std**, the output of **RR** is almost identical to the input, while stylization with **Std** changes the shape of the object introducing undesirable streaks around the outline. Thus, **RR** performs significantly better.



Figure 29: Primary shape stylization test: **RR** manages to preserve the sharp edges and clear lines of the source.

Fig. 30 shows a painterly style transfer, where both $\mathcal{L}_{\text{style}}$ and $\mathcal{L}_{\text{content}}$ are optimized. Here, the regular **Std** model mixes sky and house structures, indicating that the extracted features fail to separate style and content information. A more difficult case with a horse-to-zebra transfer is shown in Fig. 31. After optimizing $\mathcal{L}_{\text{content}}$ and $\mathcal{L}_{\text{style}}$, our method generates a zebra pattern in the horse's shadow (zoom-in in the yellow box), but yields improved results compared to a regular model. Those results indicate that **RR** is able to clearly encode the shape of the object and preserve it during the stylization, while the features of **Std** fail to clearly separate shape and style.

We additionally confirm the capabilities of the VGG model from racecar training with a low- to high-resolution transfer where the goal is purely to add detail. I.e., we can compute in-place errors w.r.t. a high-resolution reference. Both $\mathcal{L}_{\text{content}}$ and $\mathcal{L}_{\text{style}}$ are optimized and the result is shown in Fig. 32. The zoomed-in areas in the figure highlight these differences. The VGG model obtained with a regular training run yields significantly higher errors than the racecar model, as shown on the right side of Fig. 32. Here, E_{Std} contains substantially larger errors w.r.t. the reference than E_{RR} .

E Impact Statement

Racecar training could be applied to a wide range of applications, such as computer vision, computer graphics, classification tasks, generative tasks, and many more. We specifically focused on transfer learning in our paper. For regular training runs, models are trained to establish a direct relationship

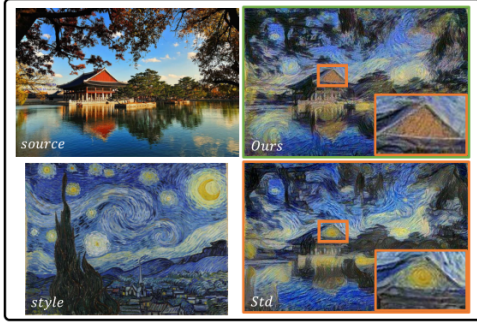


Figure 30: Stylization (natural image to van Gogh).



Figure 31: Stylization (horse to zebra).

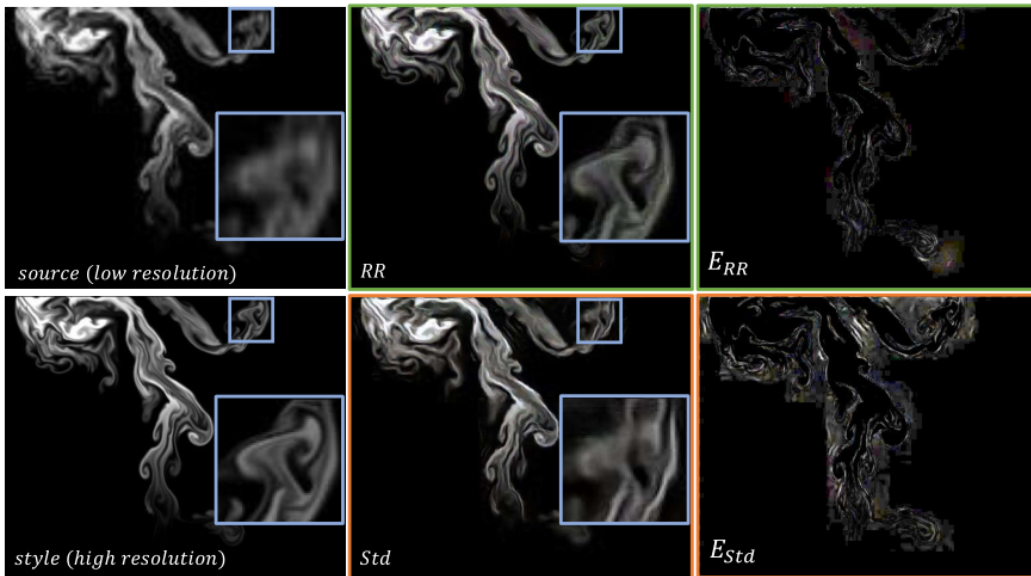


Figure 32: Comparison of stylization from low- to high-resolution simulation. Results of RR are closer to the high resolution reference.

between the input and output distribution via a specific loss function. We instead aimed at learning dominant features from the dataset via building a forward and reverse pass network. Motivated from the way humans learn, it improves the transferability of trained models. Generally, if we use the same data set for different purposes, we have to train different models from scratch. With racecar training, we can train a model which contains the dominant features of a data set as a starting point, and then reuse this model for different purposes. This is a more efficient process that likewise could be beneficial for a wide range of applications.

Besides, our research could also be used to analyze which input features are extracted by a layer, and thus improve the interpretability of neural networks in general. Hence, racecar training can be applied when the dominant features or modes of a data set are essential for making decisions about how to employ learned models.

Those properties could also result in potential risks: e.g., for data sets with personal data, i.e., in situations where privacy is critical, a learned representation using racecar training might contain more sensitive personal details than when performing a regular training. Hence, the acquired models will require additional safety measures. Thus, racecar training is, at the same time, a potential tool for analyzing the safety of a learned representation, as well as a potential risk. We encourage researchers to consider these aspects and risks arising from them for future directions of their work.

References

- [1] Lynton Ardizzone, Jakob Kruse, Sebastian Wirkert, Daniel Rahner, Eric W Pellegrini, Ralf S Klessen, Lena Maier-Hein, Carsten Rother, and Ullrich Köthe. Analyzing inverse problems with invertible neural networks. *arXiv preprint arXiv:1808.04730*, 2018.
- [2] Nitin Bansal, Xiaohan Chen, and Zhangyang Wang. Can we gain more from orthogonality regularizations in training deep cnns? In *Advances in Neural Information Processing Systems*, pages 4266–4276. Curran Associates Inc., 2018.
- [3] Saikat Basu, Manohar Karki, Sangram Ganguly, Robert DiBiano, Supratik Mukhopadhyay, Shreekanth Gayaka, Rajgopal Kannan, and Ramakrishna Nemani. Learning sparse feature representations using probabilistic quadrees and deep belief nets. *Neural Processing Letters*, 45(3):855–867, 2017.
- [4] Joan Bruna, Arthur Szlam, and Yann LeCun. Signal recovery from pooling representations. *arXiv preprint arXiv:1311.4025*, 2013.
- [5] Xi Chen, Yan Duan, Rein Houthoofd, John Schulman, Ilya Sutskever, and Pieter Abbeel. Infogan: Interpretable representation learning by information maximizing generative adversarial nets. In *Advances in Neural Information Processing Systems*, pages 2172–2180, 2016.
- [6] Kyunghyun Cho, Bart Van Merriënboer, Caglar Gulcehre, Dzmitry Bahdanau, Fethi Bougares, Holger Schwenk, and Yoshua Bengio. Learning phrase representations using rnn encoder-decoder for statistical machine translation. *arXiv preprint arXiv:1406.1078*, 2014.
- [7] Jia Deng, Wei Dong, Richard Socher, Li-Jia Li, Kai Li, and Li Fei-Fei. Imagenet: A large-scale hierarchical image database. In *IEEE conference on computer vision and pattern recognition*, pages 248–255. Ieee, 2009.
- [8] Hui Ding, Shaohua Kevin Zhou, and Rama Chellappa. Facenet2expnet: Regularizing a deep face recognition net for expression recognition. In *2017 12th IEEE International Conference on Automatic Face & Gesture Recognition (FG 2017)*, pages 118–126. IEEE, 2017.
- [9] Laurent Dinh, Jascha Sohl-Dickstein, and Samy Bengio. Density estimation using real nvp. *arXiv preprint arXiv:1605.08803*, 2016.
- [10] Mengnan Du, Ninghao Liu, and Xia Hu. Techniques for interpretable machine learning. *arXiv preprint arXiv:1808.00033*, 2018.
- [11] Lixin Duan, Dong Xu, and Ivor Tsang. Learning with augmented features for heterogeneous domain adaptation. *arXiv preprint arXiv:1206.4660*, 2012.
- [12] Marie-Lena Eckert, Kiwon Um, and Nils Thuerey. Scalarflow: a large-scale volumetric data set of real-world scalar transport flows for computer animation and machine learning. *ACM Transactions on Graphics (TOG)*, 38(6):239, 2019.
- [13] Jonathan Frankle and Michael Carbin. The lottery ticket hypothesis: Finding sparse, trainable neural networks. *arXiv preprint arXiv:1803.03635*, 2018.
- [14] Leon A Gatys, Alexander S Ecker, and Matthias Bethge. Image style transfer using convolutional neural networks. In *IEEE Conference on Computer Vision and Pattern Recognition*, pages 2414–2423, 2016.
- [15] Robert Geirhos, Patricia Rubisch, Claudio Michaelis, Matthias Bethge, Felix A Wichmann, and Wieland Brendel. Imagenet-trained cnns are biased towards texture; increasing shape bias improves accuracy and robustness. *arXiv preprint arXiv:1811.12231*, 2018.
- [16] Aidan N Gomez, Mengye Ren, Raquel Urtasun, and Roger B Grosse. The reversible residual network: Backpropagation without storing activations. In *Advances in Neural Information Processing Systems*, pages 2214–2224, 2017.
- [17] Ian Goodfellow, Jean Pouget-Abadie, Mehdi Mirza, Bing Xu, David Warde-Farley, Sherjil Ozair, Aaron Courville, and Yoshua Bengio. Generative adversarial nets. In *Advances in Neural Information Processing Systems*, pages 2672–2680, 2014.
- [18] Kasthurirangan Gopalakrishnan, Siddhartha K Khaitan, Alok Choudhary, and Ankit Agrawal. Deep convolutional neural networks with transfer learning for computer vision-based data-driven pavement distress detection. *Construction and Building Materials*, 157:322–330, 2017.
- [19] Alison Gopnik, Andrew N Meltzoff, and Patricia K Kuhl. *The scientist in the crib: Minds, brains, and how children learn*. William Morrow & Co, 1999.

- [20] Stephen José Hanson and Lorien Y Pratt. Comparing biases for minimal network construction with back-propagation. In *Advances in Neural Information Processing Systems*, pages 177–185, 1989.
- [21] Kaiming He, Xiangyu Zhang, Shaoqing Ren, and Jian Sun. Deep residual learning for image recognition. In *IEEE Conference on Computer Vision and Pattern Recognition*, pages 770–778, 2016.
- [22] Sepp Hochreiter and Jürgen Schmidhuber. Long short-term memory. *Neural computation*, 9(8):1735–1780, 1997.
- [23] Lei Huang, Xianglong Liu, Bo Lang, Adams Wei Yu, Yongliang Wang, and Bo Li. Orthogonal weight normalization: Solution to optimization over multiple dependent stiefel manifolds in deep neural networks. In *Thirty-Second AAAI Conference on Artificial Intelligence*, 2018.
- [24] Jörn-Henrik Jacobsen, Arnold Smeulders, and Edouard Oyallon. i-revnet: Deep invertible networks. *arXiv preprint arXiv:1802.07088*, 2018.
- [25] Kui Jia, Dacheng Tao, Shenghua Gao, and Xiangmin Xu. Improving training of deep neural networks via singular value bounding. In *IEEE Conference on Computer Vision and Pattern Recognition*, pages 4344–4352, 2017.
- [26] Kenji Kawaguchi, Leslie Pack Kaelbling, and Yoshua Bengio. Generalization in deep learning. *arXiv preprint arXiv:1710.05468*, 2017.
- [27] Michael Kazhdan, Thomas Funkhouser, and Szymon Rusinkiewicz. Rotation invariant spherical harmonic representation of 3 d shape descriptors. In *Symposium on geometry processing*, volume 6, pages 156–164, 2003.
- [28] Alex Krizhevsky, Geoffrey Hinton, et al. Learning multiple layers of features from tiny images. Technical report, Citeseer, 2009.
- [29] Alex Krizhevsky, Ilya Sutskever, and Geoffrey E Hinton. Imagenet classification with deep convolutional neural networks. In *Advances in Neural Information Processing Systems*, pages 1097–1105, 2012.
- [30] Anders Krogh and John A Hertz. A simple weight decay can improve generalization. In *Advances in Neural Information Processing Systems*, pages 950–957, 1992.
- [31] Brian Kulis, Kate Saenko, and Trevor Darrell. What you saw is not what you get: Domain adaptation using asymmetric kernel transforms. In *IEEE conference on computer vision and pattern recognition*, pages 1785–1792. IEEE, 2011.
- [32] Yann LeCun, Léon Bottou, Yoshua Bengio, Patrick Haffner, et al. Gradient-based learning applied to document recognition. *Proceedings of the IEEE*, 86(11):2278–2324, 1998.
- [33] Feng Li, Jacek M Zurada, Yan Liu, and Wei Wu. Input layer regularization of multilayer feedforward neural networks. *IEEE Access*, 5:10979–10985, 2017.
- [34] Aravindh Mahendran and Andrea Vedaldi. Visualizing deep convolutional neural networks using natural pre-images. *International Journal of Computer Vision*, 120(3):233–255, 2016.
- [35] Behnam Neyshabur, Srinadh Bhojanapalli, David McAllester, and Nati Srebro. Exploring generalization in deep learning. In *Advances in Neural Information Processing Systems*, pages 5947–5956, 2017.
- [36] Roman Novak, Yasaman Bahri, Daniel A Abolafia, Jeffrey Pennington, and Jascha Sohl-Dickstein. Sensitivity and generalization in neural networks: an empirical study. *arXiv preprint arXiv:1802.08760*, 2018.
- [37] Mete Ozay and Takayuki Okatani. Optimization on submanifolds of convolution kernels in cnns. *arXiv preprint arXiv:1610.07008*, 2016.
- [38] Anh Huy Phan and Andrzej Cichocki. Tensor decompositions for feature extraction and classification of high dimensional datasets. *Nonlinear theory and its applications, IEICE*, 1(1):37–68, 2010.
- [39] Peter Prettenhofer and Benno Stein. Cross-language text classification using structural correspondence learning. In *Proceedings of the 48th annual meeting of the association for computational linguistics*, pages 1118–1127, 2010.
- [40] Hariharan Ravishankar, Prasad Sudhakar, Rahul Venkataramani, Sheshadri Thiruvankadam, Pavan Annangi, Narayanan Babu, and Vivek Vaidya. Understanding the mechanisms of deep

- transfer learning for medical images. In *Deep Learning and Data Labeling for Medical Applications*, pages 188–196. Springer, 2016.
- [41] Benjamin Recht, Rebecca Roelofs, Ludwig Schmidt, and Vaishaal Shankar. Do imagenet classifiers generalize to imagenet? In *International Conference on Machine Learning*, 2019.
- [42] Ravid Shwartz-Ziv and Naftali Tishby. Opening the black box of deep neural networks via information. *arXiv preprint arXiv:1703.00810*, 2017.
- [43] Karen Simonyan and Andrew Zisserman. Very deep convolutional networks for large-scale image recognition. *arXiv preprint arXiv:1409.1556*, 2014.
- [44] Nitish Srivastava, Geoffrey Hinton, Alex Krizhevsky, Ilya Sutskever, and Ruslan Salakhutdinov. Dropout: a simple way to prevent neural networks from overfitting. *The journal of machine learning research*, 15(1):1929–1958, 2014.
- [45] S-H Tang, Gang Chen, and Y-S Ma. Fundamental concepts of generic features. In *Semantic modeling and interoperability in product and process engineering*, pages 89–115. Springer, 2013.
- [46] Yunfei Teng and Anna Choromanska. Invertible autoencoder for domain adaptation. *Computation*, 7(2):20, 2019.
- [47] Nils Thuerey and Tobias Pfaff. MantaFlow, 2018. <http://mantaflow.com>.
- [48] Naftali Tishby and Noga Zaslavsky. Deep learning and the information bottleneck principle. In *2015 IEEE Information Theory Workshop (ITW)*, pages 1–5. IEEE, 2015.
- [49] Lisa Torrey and Jude Shavlik. Transfer learning. In *Handbook of research on machine learning applications and trends: algorithms, methods, and techniques*, pages 242–264. IGI Global, 2010.
- [50] Michael E Wall, Andreas Rechtsteiner, and Luis M Rocha. Singular value decomposition and principal component analysis. In *A practical approach to microarray data analysis*, pages 91–109. Springer, 2003.
- [51] Janett Walters-Williams and Yan Li. Estimation of mutual information: A survey. In *International Conference on Rough Sets and Knowledge Technology*, pages 389–396. Springer, 2009.
- [52] Andreas S Weigend, David E Rumelhart, and Bernardo A Huberman. Generalization by weight-elimination with application to forecasting. In *Advances in Neural Information Processing Systems*, pages 875–882, 1991.
- [53] You Xie, Erik Franz, Mengyu Chu, and Nils Thuerey. tempogan: A temporally coherent, volumetric gan for super-resolution fluid flow. *ACM Transactions on Graphics (TOG)*, 37(4):95, 2018.
- [54] Amir R Zamir, Alexander Sax, William Shen, Leonidas J Guibas, Jitendra Malik, and Silvio Savarese. Taskonomy: Disentangling task transfer learning. In *IEEE Conference on Computer Vision and Pattern Recognition*, pages 3712–3722, 2018.
- [55] Matthew D Zeiler and Rob Fergus. Visualizing and understanding convolutional networks. In *European conference on computer vision*, pages 818–833. Springer, 2014.
- [56] Lijing Zhang, Yao Lu, Ge Song, and Hanfeng Zheng. Rc-cnn: Reverse connected convolutional neural network for accurate player detection. In *Pacific Rim International Conference on Artificial Intelligence*, pages 438–446. Springer, 2018.
- [57] Richard Zhang, Phillip Isola, Alexei A Efros, Eli Shechtman, and Oliver Wang. The unreasonable effectiveness of deep features as a perceptual metric. In *IEEE Conference on Computer Vision and Pattern Recognition*, pages 586–595, 2018.
- [58] Joey Tianyi Zhou, Sinno Jialin Pan, Ivor W Tsang, and Yan Yan. Hybrid heterogeneous transfer learning through deep learning. In *Twenty-eighth AAAI conference on artificial intelligence*, 2014.
- [59] Joey Tianyi Zhou, Ivor W Tsang, Sinno Jialin Pan, and Mingkui Tan. Heterogeneous domain adaptation for multiple classes. In *Artificial Intelligence and Statistics*, pages 1095–1103, 2014.
- [60] Yin Zhu, Yuqiang Chen, Zhongqi Lu, Sinno Jialin Pan, Gui-Rong Xue, Yong Yu, and Qiang Yang. Heterogeneous transfer learning for image classification. In *Twenty-Fifth AAAI Conference on Artificial Intelligence*, 2011.

Table 1. Model Accuracy of MI Source Task

Training Runs	Std_A	Ort_A	RR_A^1	IRR_A	RR_A	Std_{AA}	Ort_{AA}	RR_{AA}^1	IRR_{AA}	RR_{AA}
1	0.976	0.969	0.836	0.8350	0.772	0.978	0.968	0.885	0.9770	0.992
2	0.975	0.921	0.68	0.8360	0.784	0.983	0.926	0.918	0.9770	0.994
3	0.964	0.957	0.8	0.8140	0.725	0.963	0.958	0.993	0.9740	0.993
4	0.987	0.991	0.657	0.8420	0.771	0.989	0.993	0.917	0.9980	0.989
5	0.957	0.979	0.825	0.8400	0.774	0.954	0.979	0.944	0.9710	0.993
Avg.	0.972	0.963	0.760	0.8334	0.765	0.973	0.965	0.931	0.9794	0.992
Std. dev.	0.012	0.027	0.085	0.0112	0.023	0.015	0.025	0.040	0.0107	0.002

Table 2. Model Accuracy of MI Transfer Task

Training Runs	Std_{AB}	Ort_{AB}	Std_B	RR_{AB}^1	IRR_{AB}	RR_{AB}
1	0.136	0.984	0.852	0.919	0.998	0.998
2	0.136	0.136	0.991	0.954	0.991	0.997
3	0.989	0.957	0.953	0.977	0.978	0.995
4	0.136	0.991	0.909	0.963	0.989	0.997
5	0.96	0.977	0.965	0.963	0.969	1.000
Avg.	0.471	0.809	0.934	0.955	0.9850	0.997
Std. dev.	0.459	0.376	0.055	0.022	0.0115	0.002

Table 3. Model Accuracy of MNIST Source Task

Training Runs	Ort_{mni}	Std_{mni}	RR_{mni}	Ort_{MNI}	Std_{MNI}	RR_{MNI}
1	0.9792	0.9827	0.981	0.9819	0.9854	0.9856
2	0.8322	0.9815	0.9824	0.982	0.9837	0.9851
3	0.9511	0.9815	0.9828	0.9792	0.983	0.9862
4	0.8841	0.9817	0.9816	0.9814	0.9842	0.9867
5	0.8266	0.9829	0.9816	0.9816	0.9846	0.9861
Avg.	0.895	0.982	0.982	0.981	0.984	0.986
Std. dev.	0.0689	0.0007	0.0007	0.0011	0.0009	0.0006

Table 4. Model Accuracy of MNIST Transfer Task

Training Runs	Ort_{n-M}	Std_{n-MNI}	RR_{n-MNI}	$Std_{n-MNI-fs}$
1	0.949	0.956	0.9612	0.8714
2	0.8629	0.9458	0.954	0.9657
3	0.9458	0.9543	0.9648	0.9659
4	0.9495	0.9559	0.9604	0.8789
5	0.8564	0.9466	0.9649	0.9638
Avg.	0.913	0.952	0.961	0.929
Std. dev.	0.0485	0.0051	0.0044	0.0494

Table 5. Model Accuracy of CIFAR Tests (19 layers network)

Training Runs	Std_{c1}	RR_{c1}	Std_{c10}	RR_{c10}	Std_{c100}	RR_{c100}	$Std_{c100-fs}$
1	0.8263	0.5784	0.8351	0.869	0.2063	0.2602	0.2581
2	0.7868	0.5553	0.7936	0.8538	0.1838	0.2687	0.2659
3	0.7729	0.7686	0.7718	0.8449	0.1795	0.2803	0.2386
4	0.865	0.7382	0.8472	0.8692	0.1738	0.2969	0.2418
5	0.781	0.6775	0.7787	0.8418	0.1704	0.2733	0.2621
Avg.	0.806	0.664	0.805	0.856	0.183	0.276	0.253
Std. dev.	0.0387	0.0945	0.0340	0.0130	0.0141	0.0138	0.0123

Table 6. Model L^2 Loss of Smoke Tests. Results for $B_2: 10^7$

Training Runs	Std_{AB_1}	RR_{AB_1}	Std_{B_1}	Std_{AB_2}	RR_{AB_2}	Std_{B_2}
1	338.4	197.7	22291	1.93	1.62	2.84
2	380.2	203.6	22883	1.63	1.55	2.84
3	2096.2	206	31911	2.40	1.56	2.81
4	214.3	203.1	31807	1.52	1.54	2.84
5	219.9	200.8	34441	1.49	1.51	2.84
Avg.	649.8	202.24	28666.6	1.80	1.56	2.84
Std. dev.	811.82	3.14	5653.1	0.382	0.0381	0.012

Table 7. Model Accuracy of CIFAR Tests (Resnet 110 network)

Training Runs	Std_{c1}	Ort_{c1}	RR_{c1}	Std_{c1}	Ort_{c10}	RR_{c1}	Std_{c1}	Ort_{c10}	RR_{c10}
	CIFAR 10					CIFAR 10.1			
1	0.9082	0.9042	0.9076	0.9194	0.9255	0.9277	0.8275	0.8375	0.8435
2	0.909	0.9081	0.9026	0.9228	0.9231	0.9267	0.8315	0.8315	0.846
3	0.908	0.9085	0.9028	0.92	0.9239	0.927	0.8305	0.8415	0.834
4	0.9031	0.9098	0.9052	0.9176	0.9257	0.928	0.8325	0.8395	0.8335
5	0.9104	0.9106	0.9108	0.9249	0.9259	0.9286	0.835	0.8435	0.8475
Avg.	0.9077	0.9082	0.9058	0.9209	0.9248	0.9276	0.8314	0.8387	0.8409
Std. dev.	0.0028	0.0025	0.0035	0.0029	0.0012	0.0008	0.0027	0.0046	0.0067

Table 8. Forward and Reverse Pass Neural Networks for MNIST and *peak* Tests

<p>Forward pass: <i>MNIST</i> (Fig. 1): $I(784) \rightarrow FC(10) + b_1 \rightarrow O(10)$. <i>peak</i> (Fig. 2 & Fig.4 (a)): $I(784) \rightarrow FC(2) + b_1 \rightarrow O(2)$. <i>peak</i> (Fig. 4 (b)): $I(784) \rightarrow relu(BN(FC(2) + b_1)) \rightarrow O(2)$. <i>peak</i> (Fig. 4 (c)): $I(784) \rightarrow relu(BN(FC(128) + b_1)) \rightarrow relu(BN(FC(2) + b_2)) \rightarrow O(2)$.</p>
<p>Reverse pass: <i>MNIST</i> (Fig. 1): $I(10) - b_1 \rightarrow FC(784) \rightarrow O(784)$ <i>peak</i> (Fig. 2 & Fig.4 (a)): $I(10) - b_1 \rightarrow FC(784) \rightarrow O(784)$ <i>peak</i> (Fig. 4 (b)): $I(2) - b_1 \rightarrow FC(784) \rightarrow O(784)$. <i>peak</i> (Fig. 4 (c)): $I(2) - b_2 \rightarrow relu(BN(FC(128)) - b_1 \rightarrow FC(784) \rightarrow O(784)$.</p>

Table 9. Forward and Reverse Pass Neural Network for MI Tests

<p>Forward pass: $I(12) \rightarrow tanh(FC(10) + b_1) = d_1 \rightarrow tanh(FC(7) + b_2) = d_2 \rightarrow tanh(FC(5) + b_3) = d_3$ $\rightarrow tanh(FC(4) + b_4) = d_4 \rightarrow tanh(FC(3) + b_5) = d_5 \rightarrow tanh(FC(2) + b_6) = d_6 \rightarrow O(2)$.</p>
<p>Reverse pass (RR_A): $I(2) - b_6 \rightarrow tanh(FC(3)) - b_5 \rightarrow tanh(FC(4)) - b_4 \rightarrow tanh(FC(5)) - b_3 \rightarrow tanh(FC(7)) - b_2$ $\rightarrow tanh(FC(10)) - b_1 \rightarrow tanh(FC(12)) \rightarrow O(12)$.</p>
<p>Reverse pass (IRR_A): $d_6 - b_6 \rightarrow tanh(FC(3)) = d'_5, d_5 - b_5 \rightarrow tanh(FC(4)) = d'_4, d_4 - b_4 \rightarrow tanh(FC(5)) = d'_3,$ $d_3 - b_3 \rightarrow tanh(FC(7)) = d'_2, d_2 - b_2 \rightarrow tanh(FC(10)) = d'_1, d_1 - b_1 \rightarrow tanh(FC(12)) = d'_0$</p>

Table 10. Hyperparameters of MI Tests

Batch Size	512	Learning Rate	0.0004
λ	$RR_A: \lambda_{1-6} = 10^{-2}$ $IRR_A: \lambda_1 = 8 \times 10^{-2}, \lambda_2 = 6 \times 10^{-2}, \lambda_3 = 4 \times 10^{-2}, \lambda_4 = 2 \times 10^{-2}, \lambda_{1,2} = 10^{-2}$		
Training Epochs	20000 for $RR_{A/AA/AB}, IRR_{A/AA/AB}, Std_{A/AA/AB}$ and Std_B		

Table 11. Forward and Reverse Pass Neural Network for Digit Generation Tests

<p>Forward pass: $I(74) \rightarrow relu(BN(FC(1024))) \rightarrow relu(BN(FC(6272))) \rightarrow relu(BN(C(4,64,2))) \rightarrow relu(BN(C(4,1,2))) = I_r$.</p>
<p>Reverse pass ($RR_{A/AA/AB}$): $I_r \rightarrow relu(BN(D(4,64,2))) \rightarrow relu(BN(D(4,128,2))) \rightarrow relu(BN(FC(1024))) \rightarrow relu(FC(74)) \rightarrow O(74)$.</p>

Table 12. Hyperparameters of Digit Generation Tests

Batch Size	256	λ	$\lambda_{c1} = 2 \times 10^{-3}; \lambda_{c2,3} = 1.5 \times 10^{-3}$
Learning Rate	0.001 for RR^1 and Std	Training Steps	150000 steps for RR^1 and Std

Table 13. Forward and Reverse Pass Network for Texture-shape Tests

<p>Forward pass: $I(224,224,3) \rightarrow relu(C(4,8,2) + b_1) \rightarrow relu(C(4,8,2) + b_2) \rightarrow relu(C(4,8,2) + b_3) \rightarrow relu(C(4,8,2) + b_4)$ $\rightarrow relu(C(4,8,2) + b_5) \rightarrow relu(C(4,8,1) + b_6) = I_r \rightarrow FC(16) \rightarrow O(16)$</p>
<p>Reverse pass: $I_r - b_6 \rightarrow relu(D(4,8,1)) - b_5 \rightarrow relu(D(4,8,2)) - b_4 \rightarrow relu(D(4,8,2)) - b_3 \rightarrow relu(D(4,8,2)) - b_2$ $\rightarrow relu(D(4,8,2)) - b_1 \rightarrow relu(D(4,3,2)) \rightarrow O(224,224,3)$</p>

Table 14. Hyperparameters of Texture-shape Tests

Batch Size	64	λ_{1-6}	5×10^{-1}
Learning Rate	0.0001	Training Epochs	200

Table 15. Forward and Reverse Pass Neural Network for MNIST Classification Tests

Forward pass: $I(28,28,1) \rightarrow \text{relu}(C(3,64,1) + b_1) \rightarrow MP \rightarrow \text{relu}(C(3,64,1) + b_2) \rightarrow MP \rightarrow \text{relu}(C(3,1,1) + b_3) = I_r$ $\rightarrow FC(10) \rightarrow O(10)$
Reverse pass: $I_r - b_3 \rightarrow \text{relu}(D(3,64,1)) \rightarrow UP - b_2 \rightarrow \text{relu}(D(3,64,1)) \rightarrow UP - b_1 \rightarrow \text{relu}(D(3,1,1)) \rightarrow O(28,28,1)$

Table 16. Hyperparameters of MNIST Classification Tests

Batch Size	64	λ_{1-3}	10^{-5}
Learning Rate	0.001 for RR_{mni}, Std_{mni} and Ort_{mni} ; 0.0001 for $RR_{MNI/n-MNI}, Std_{MNI/n-MN}$ and $Ort_{MNI/n-MNI}$.		
Training Epochs	100 for RR_{mni}, Std_{mni} and Ort_{mni} ; 400 for RR_{MNI}, Std_{MNI} and Ort_{MNI} ; 700 for RR_{n-MN}, Std_{n-MN} and Ort_{n-MNI} .		

Table 17. Forward and Reverse Pass Neural Network for CIFAR Tests (Resnet 110 network)

Example residual block in forward pass: $I(32,32,3) \rightarrow \dots \rightarrow BN, \text{relu} \rightarrow d_{min} \rightarrow C(3,64,1) \rightarrow d_{mout} \rightarrow BN, \text{relu} \rightarrow d_{m+1in} \rightarrow C(3,64,1) \rightarrow d_{m+1out} \rightarrow \oplus \rightarrow \dots$
Example block in reverse pass: $d_{m+1out} \rightarrow D(3,64,1) \rightarrow d'_{m+1in}, d'_{mout} \rightarrow D(3,64,1) \rightarrow d'_{min}, \dots$

Table 18. Hyperparameters of CIFAR Tests (Resnet 110 network)

Batch Size	256	λ	10^{-8}	Training Epochs	200 epochs
Learning Rate	RR_{c1}, Ort_{c1} and Std_{c1} : 0.01 RR_{c1}, Ort_{c1} and Std_{c10} : 0.01 (0-80 epochs), 0.001 (80-120 epochs) 0.0001 (120-160 epochs), 0.00001 (160-200 epochs)				

Table 19. Forward and Reverse Pass Neural Network for CIFAR Tests (19 layers network)

Forward pass: $I(32,32,3) \rightarrow \text{relu}(BN(C(3,64,1) + b_1)) \rightarrow \text{relu}(BN(C(3,64,1) + b_2)) \rightarrow MP$ $\rightarrow \text{relu}(BN(C(3,128,1) + b_3)) \rightarrow \text{relu}(BN(C(3,128,1) + b_4)) \rightarrow MP \rightarrow \text{relu}(BN(C(3,256,1) + b_5))$ $\rightarrow \text{relu}(BN(C(3,256,1) + b_6)) \rightarrow \text{relu}(BN(C(3,256,1) + b_7)) \rightarrow MP \rightarrow \text{relu}(BN(C(3,512,1) + b_8))$ $\rightarrow \text{relu}(BN(C(3,512,1) + b_9)) \rightarrow \text{relu}(BN(C(3,512,1) + b_{10})) \rightarrow MP \rightarrow \text{relu}(BN(C(3,512,1) + b_{11}))$ $\rightarrow \text{relu}(BN(C(3,512,1) + b_{12})) \rightarrow \text{relu}(BN(C(3,512,1) + b_{13})) = I_r \rightarrow \text{relu}(BN(FC(4096) + b_{14}))$ $\rightarrow \text{relu}(BN(FC(4096) + b_{15})) \rightarrow \text{relu}(BN(FC(10) + b_{16})) \rightarrow O(10)$.
Reverse pass: $I_r - b_{13} \rightarrow \text{relu}(BN(D(3,512,1))) - b_{12} \rightarrow \text{relu}(BN(D(3,512,1))) - b_{11} \rightarrow \text{relu}(BN(D(3,512,1)))$ $\rightarrow UP - b_{10} \rightarrow \text{relu}(BN(D(3,512,1))) - b_9 \rightarrow \text{relu}(BN(D(3,512,1))) - b_8 \rightarrow \text{relu}(BN(D(3,256,1)))$ $\rightarrow UP - b_7 \rightarrow \text{relu}(BN(D(3,256,1))) - b_6 \rightarrow \text{relu}(BN(D(3,256,1))) - b_5 \rightarrow \text{relu}(BN(D(3,128,1)))$ $\rightarrow UP - b_4 \rightarrow \text{relu}(BN(D(3,128,1))) - b_3 \rightarrow \text{relu}(BN(D(3,64,1))) \rightarrow UP - b_2$ $\rightarrow \text{relu}(BN(D(3,64,1))) - b_1 \rightarrow \text{relu}(D(3,3,1)) \rightarrow O(32,32,3)$.

Table 20. Hyperparameters of CIFAR Tests (19 layers network)

Batch Size	200	λ_{1-3}	10^{-7}
Learning Rate	0.1 (0 to 80epochs); 0.01 (81 to epochs); 0.001 (after 120 epochs).	Training Epochs	180 for $RR_{c1/c10}$ and $Std_{c1/c10}$; 50 for RR_{c100} and $Std_{c100/c100-fs}$.

Table 21. Forward and Reverse Pass Neural Network for Smoke Tests

Generator forward pass: $I(16,16,1) \rightarrow \text{relu}(C(5,64,1) + b_1) \rightarrow UP \rightarrow \text{relu}(C(5,128,1) + b_2) \rightarrow UP \rightarrow \text{relu}(C(5,128,1) + b_3)$ $\rightarrow \text{relu}(C(5,64,1) + b_4) \rightarrow \text{relu}(C(5,32,1) + b_5) \rightarrow \text{relu}(C(5,1,1) + b_6) \rightarrow O(64,64,1) = I_r$.
Generator reverse pass: $I_r - b_6 \rightarrow \text{relu}(D(5,32,1)) - b_5 \rightarrow \text{relu}(D(5,64,1)) - b_4 \rightarrow \text{relu}(D(5,128,1)) - b_3 \rightarrow \text{relu}(D(5,128,1))$ $\rightarrow MP - b_2 \rightarrow \text{relu}(D(5,64,1)) \rightarrow MP - b_1 \rightarrow \text{relu}(D(5,1,1)) \rightarrow O(16,16,1)$.
Discriminator: $I(64,64,2) \rightarrow \text{lrelu}(BN(C(5,32,1) + b_1)) \rightarrow \text{lrelu}(BN(C(5,64,1) + b_2))$ $\rightarrow \text{lrelu}(BN(C(5,128,1) + b_3)) \rightarrow \text{lrelu}(BN(C(5,256,1) + b_4)) \rightarrow FC(1) + b_5 \rightarrow O(1)$.

Table 22. Autoencoder Architecture for Smoke Tests

<p><i>Std_{AB₁}</i>: $I(64,64,1) \rightarrow \text{relu}(C(5,32,1) + b_1) \rightarrow \text{relu}(C(5,64,1) + b_2) \rightarrow \text{relu}(C(5,128,1) + b_3)$ $\rightarrow \text{relu}(C(5,128,1) + b_4) \rightarrow MP \rightarrow \text{relu}(C(5,64,1) + b_5) \rightarrow MP \rightarrow \text{relu}(C(5,1,1) + b_6)$ $\rightarrow \text{relu}(C(5,64,1) + b_7) \rightarrow UP \rightarrow \text{relu}(C(5,128,1) + b_8) \rightarrow UP \rightarrow \text{relu}(C(5,128,1) + b_9)$ $\rightarrow \text{relu}(C(5,64,1) + b_{10}) \rightarrow \text{relu}(C(5,32,1) + b_{11}) \rightarrow \text{relu}(C(5,1,1) + b_{12}) \rightarrow O(64,64,1).$</p>
<p><i>RR_{AB₁}</i>: $I(64,64,1) - b_1 \rightarrow \text{relu}(D(5,32,1)) - b_2 \rightarrow \text{relu}(D(5,64,1)) - b_3 \rightarrow \text{relu}(D(5,128,1)) - b_4$ $\rightarrow \text{relu}(C(5,128,1)) \rightarrow MP - b_5 \rightarrow \text{relu}(D(5,64,1)) \rightarrow MP - b_6 \rightarrow \text{relu}(D(5,1,1))$ $\rightarrow \text{relu}(C(5,64,1) + b_7) \rightarrow UP \rightarrow \text{relu}(C(5,128,1) + b_8) \rightarrow UP \rightarrow \text{relu}(C(5,128,1) + b_9)$ $\rightarrow \text{relu}(C(5,64,1) + b_{10}) \rightarrow \text{relu}(C(5,32,1) + b_{11}) \rightarrow \text{relu}(C(5,1,1) + b_{12}) \rightarrow O(64,64,1).$</p>
<p><i>Std_{AB₂} and RR_{AB₂}</i>: $I(64,64,3) \rightarrow \text{relu}(C(5,32,1) + b_1) \rightarrow \text{relu}(C(5,64,1) + b_2) \rightarrow \text{relu}(C(5,128,1) + b_3)$ $\rightarrow \text{relu}(C(5,128,1) + b_4) \rightarrow MP \rightarrow \text{relu}(C(5,64,1) + b_5) \rightarrow MP \rightarrow \text{relu}(C(5,1,1) + b_6)$ $\rightarrow \text{relu}(C(5,64,1) + b_7) \rightarrow UP \rightarrow \text{relu}(C(5,128,1) + b_8) \rightarrow UP \rightarrow \text{relu}(C(5,128,1) + b_9)$ $\rightarrow \text{relu}(C(5,64,1) + b_{10}) \rightarrow \text{relu}(C(5,32,1) + b_{11}) \rightarrow \text{relu}(C(5,3,1) + b_{12}) \rightarrow O(64,64,3).$</p>

Table 23. Hyperparameters of Smoke Tests

Batch Size	64	Learning Rate	0.0002	λ	$\lambda_1 = 10; \lambda_{2-6} = 0.1$
Training Epochs	40000 for <i>RR_A</i> and <i>Std_A</i> ; 1000 for <i>RR_{AB₁}</i> , <i>RR_{AB₂}</i> , <i>Std_{AB₁}</i> and <i>Std_{AB₂}</i> .				

Table 24. Forward and Reverse Pass Neural Network for VGG19 Network

<p>Forward pass: $I(224,224,3) \rightarrow \text{relu}(C(3,64,1) + b_1) \rightarrow \text{relu}(C(3,64,1) + b_2) \rightarrow MP \rightarrow \text{relu}(C(3,128,1) + b_3)$ $\rightarrow \text{relu}(C(3,128,1) + b_4) \rightarrow MP \rightarrow \text{relu}(C(3,256,1) + b_5) \rightarrow \text{relu}(C(3,256,1) + b_6)$ $\rightarrow \text{relu}(C(3,256,1) + b_7) \rightarrow \text{relu}(C(3,256,1) + b_8) \rightarrow MP \rightarrow \text{relu}(C(3,512,1) + b_9)$ $\rightarrow \text{relu}(C(3,512,1) + b_{10}) \rightarrow \text{relu}(C(3,512,1) + b_{11}) \rightarrow \text{relu}(C(3,512,1) + b_{12}) \rightarrow MP$ $\rightarrow \text{relu}(C(3,512,1) + b_{13}) \rightarrow \text{relu}(C(3,512,1) + b_{14}) \rightarrow \text{relu}(C(3,512,1) + b_{15})$ $\rightarrow \text{relu}(C(3,512,1) + b_{16}) = I_r \rightarrow MP \rightarrow \text{relu}(FC(4096) + b_{17}) \rightarrow \text{relu}(FC(4096) + b_{18})$ $\rightarrow \text{relu}(FC(1000) + b_{19}) \rightarrow O(1000).$</p>
<p>Reverse pass: $I_r - b_{16} \rightarrow \text{relu}(D(3,512,1)) - b_{15} \rightarrow \text{relu}(D(3,512,1)) - b_{14} \rightarrow \text{relu}(D(3,512,1)) - b_{13}$ $\rightarrow \text{relu}(D(3,512,1)) \rightarrow UP - b_{12} \rightarrow \text{relu}(D(3,512,1)) - b_{11} \rightarrow \text{relu}(D(3,512,1)) - b_{10}$ $\rightarrow \text{relu}(D(3,512,1)) - b_9 \rightarrow \text{relu}(D(3,256,1)) \rightarrow UP - b_8 \rightarrow \text{relu}(D(3,256,1)) - b_7$ $\rightarrow \text{relu}(D(3,256,1)) - b_6 \rightarrow \text{relu}(D(3,256,1)) - b_5 \rightarrow \text{relu}(D(3,128,1)) \rightarrow UP - b_4$ $\rightarrow \text{relu}(D(3,128,1)) - b_3 \rightarrow \text{relu}(D(3,64,1)) \rightarrow UP - b_2 \rightarrow \text{relu}(D(3,64,1)) - b_1 \rightarrow \text{relu}(D(3,3,1))$ $\rightarrow O(224,224,3).$</p>

Table 25. Hyperparameters of VGG19 Training

λ_{1-16}	10^{-10}
Learning Rate	0.01 (0 to 7 epochs); 0.001 (7 to 10 epochs); 0.0001(10 to 15 epochs); 0.00001 (after 15 epochs).
Training Epochs	36 epochs for <i>RR_{VGG}</i> and <i>Std_{VGG}</i> ; 22 epochs for <i>RR</i> and <i>Std</i> .

Table 26. $I(X; \mathcal{D}_m)$ and $I(\mathcal{D}_m; Y)$ Values of All MI Models

	Results of 5 runs	$I(X; \mathcal{D}_2)$	$I(X; \mathcal{D}_3)$	$I(X; \mathcal{D}_4)$	$I(X; \mathcal{D}_5)$	$I(X; \mathcal{D}_6)$	$I(X; \mathcal{D}_7)$	$I(\mathcal{D}_2; Y)$	$I(\mathcal{D}_3; Y)$	$I(\mathcal{D}_4; Y)$	$I(\mathcal{D}_5; Y)$	$I(\mathcal{D}_6; Y)$	$I(\mathcal{D}_7; Y)$
Std_A	Avg.	11.9992	11.9879	11.7279	7.9088	2.9612	1.2367	0.9992	0.9992	0.9973	0.9947	0.9786	0.9554
	Std. dev.	0.0011	0.0138	0.2007	1.5376	0.8695	0.0973	0.0000	0.0000	0.0012	0.0031	0.0112	0.0233
RR_A^1	Avg.	11.5487	10.3822	8.8948	7.8285	6.1742	3.9528	0.9564	0.8418	0.7463	0.6921	0.5969	0.4937
	Std. dev.	0.9988	1.1225	0.5715	0.7409	0.7583	0.2322	0.0940	0.0785	0.0440	0.0131	0.0652	0.0736
IRR_A	Avg.	11.5521	6.7737	4.0047	4.0087	3.8456	3.7120	0.9388	0.6372	0.6013	0.6002	0.6008	0.5997
	Std. dev.	0.0558	2.3736	0.1872	0.2787	0.2033	0.0909	0.0070	0.0334	0.0244	0.0233	0.0231	0.0236
RR_A	Avg.	5.2845	4.8838	4.2668	3.9356	4.7603	4.6238	0.5654	0.5369	0.5358	0.5182	0.5261	0.5336
	Std. dev.	0.4545	0.1569	0.3115	0.1279	0.0783	0.0173	0.0337	0.0039	0.0111	0.0060	0.0115	0.0031
Ort_A	Avg.	11.9976	11.9702	11.4784	7.7023	2.6314	1.0755	0.9992	0.9992	0.9955	0.9849	0.9681	0.9493
	Std. dev.	0.0051	0.0505	0.5529	0.8500	0.4071	0.0629	0.0000	0.0000	0.0054	0.0128	0.0254	0.0325
Std_{AA}	Avg.	11.9984	11.9770	11.7029	7.3237	2.6905	1.2204	0.9992	0.9990	0.9973	0.9932	0.9752	0.9583
	Std. dev.	0.0021	0.0292	0.2305	1.2948	0.3707	0.1700	0.0000	0.0004	0.0009	0.0080	0.0169	0.0242
RR_{AA}^1	Avg.	11.9989	11.8699	11.0450	9.0914	3.9232	1.3239	0.9992	0.9934	0.9813	0.9778	0.9404	0.9054
	Std. dev.	0.0016	0.2075	0.9404	1.8047	1.3972	0.4193	0.0000	0.0118	0.0217	0.0374	0.0420	0.0528
IRR_{AA}	Avg.	11.9527	10.2473	8.1597	6.7212	2.4402	1.1113	0.9992	0.9743	0.9662	0.9917	0.9859	0.9706
	Std. dev.	0.0472	1.6567	2.3965	1.8774	0.4665	0.0512	0.0000	0.0227	0.0124	0.0047	0.0110	0.0197
RR_{AA}	Avg.	11.9200	11.5621	10.6095	7.7398	2.2372	1.0416	0.9992	0.9988	0.9985	0.9975	0.9906	0.9875
	Std. dev.	0.0540	0.1463	0.5465	0.8093	1.0104	0.0505	0.0000	0.0005	0.0007	0.0024	0.0073	0.0046
Ort_{AA}	Avg.	11.9970	11.9727	11.3343	6.1690	1.9642	1.0985	0.9992	0.9991	0.9971	0.9832	0.9625	0.9477
	Std. dev.	0.0061	0.0504	0.6796	1.2529	0.5865	0.0891	0.0000	0.0002	0.0032	0.0166	0.0269	0.0320
Std_{AB}	Avg.	11.9989	11.9794	10.2985	3.0652	1.2677	0.5283	0.9992	0.9988	0.9029	0.4041	0.3923	0.3860
	Std. dev.	0.0019	0.0116	1.5095	4.0345	1.8717	0.7445	0.0000	0.0006	0.0918	0.5359	0.5329	0.5288
RR_{AB}^1	Avg.	11.9895	11.7982	9.7800	7.4955	3.2139	1.3122	0.9992	0.9901	0.9644	0.9661	0.9472	0.9308
	Std. dev.	0.0075	0.1710	1.0207	1.4405	1.2750	0.1537	0.0000	0.0131	0.0310	0.0357	0.0349	0.0344
IRR_{AB}	Avg.	11.9047	10.8970	8.3860	5.4257	1.7110	1.0694	0.9989	0.9915	0.9813	0.9929	0.9812	0.9735
	Std. dev.	0.0890	0.8474	1.9089	1.1511	0.4913	0.0529	0.0006	0.0089	0.0145	0.0085	0.0209	0.0235
RR_{AB}	Avg.	11.9093	11.5761	9.4227	5.6190	2.2286	1.0100	0.9992	0.9992	0.9984	0.9989	0.9962	0.9935
	Std. dev.	0.0957	0.1450	1.7109	1.4609	0.4611	0.0091	0.0000	0.0000	0.0014	0.0004	0.0032	0.0035
Ort_{AB}	Avg.	11.9946	11.9546	8.9865	3.2802	1.4296	0.8571	0.9992	0.9985	0.8048	0.7851	0.7756	0.7675
	Std. dev.	0.0104	0.0561	3.3571	2.7102	0.9848	0.4858	0.0000	0.0007	0.4279	0.4391	0.4342	0.4296
Std_B	Avg.	12.0000	11.9913	11.7602	8.6184	3.2490	1.3171	0.9992	0.9990	0.9975	0.9880	0.9458	0.9160
	Std. dev.	0.0000	0.0113	0.3400	2.0542	1.2740	0.2025	0.0000	0.0003	0.0007	0.0114	0.0476	0.0565

Table 27. Per Category Accuracy of RR_A for Texture-shape Tests

Data Sets		stylized data																edge data		filled data
Model	Runs	airplane	bear	bicycle	bird	boat	bottle	car	cat	chair	clock	dog	elephant	keyboard	knife	oven	truck	Acc.	Acc.	Acc.
RR_{T5}	0	0.9	0	0.7	0.6	0	0.9	0.6	0.8	0.2	0.7	0	1	0.6	0.5	0	0.8	0.5214	0.3063	0.4500
	1	0.9	0.6	0	0.4	0.7	1	0	0.9	0.5	0	0.4	0	0.7	0.5	0.9	1	0.5145	0.2813	0.4375
	2	1	0.9	1	0.6	0.8	0	0.7	0	0.7	0.9	0.5	0.8	0	0	0.9	0.6043	0.1938	0.4500	
	3	0	0.8	1	0.9	0.5	0	1	0	0	0	0.3	0	0.9	0.7	0.9	0	0.4402	0.2125	0.3313
	4	0.8	0.9	0	0.7	0.5	1	0	0.5	0	0.9	0	1	0.4	0.7	0.8	1	0.5746	0.2125	0.3625
	5	0.9	0.7	0.8	0	0	1	1	0	1	0.8	0.6	0	1	0.9	0.8	1	0.6471	0.2500	0.4563
	6	0.9	0.9	0.9	0.9	0.4	0.9	0.8	0.4	0.6	0.8	0.3	0	0	0	0	1	0.5465	0.2563	0.4375
	7	1	0.9	0.8	0.7	0.6	0	0.3	0.7	0	0.9	0.6	0.4	0	0.8	0.8	1	0.5897	0.2813	0.4313
	8	0.8	0.6	0	0.5	0.5	0	0.6	0.8	0	0.8	0.3	0	0.6	0.8	0.7	0.8	0.4850	0.1813	0.3563
	9	0.7	0.8	0	0.8	0	1	0	0.9	0	0.9	0.5	1	0.9	0.7	0.7	0	0.5440	0.1938	0.3625
Avg.	0.79	0.71	0.52	0.61	0.4	0.58	0.5	0.5	0.3	0.67	0.35	0.42	0.51	0.56	0.66	0.75	0.5467	0.2369	0.4075	
Std. dev.	0.2923	0.2767	0.4566	0.2685	0.2981	0.5007	0.4000	0.3801	0.3712	0.3592	0.2173	0.4756	0.3929	0.3204	0.3596	0.4035	0.0604	0.0438	0.0481	

Table 28. Per Category Accuracy of Ort_A for Texture-shape Tests

Data Sets		stylized data																edge data		filled data
Model	Runs	airplane	bear	bicycle	bird	boat	bottle	car	cat	chair	clock	dog	elephant	keyboard	knife	oven	truck	Acc.	Acc.	Acc.
Ort_{T5}	0	0.7	0	0.8	0.3	0	1	0.7	0.8	0.5	0	0.4	0.5	0.7	0.5	0.9	0	0.4987	0.1688	0.4188
	1	0.6	0.3	0.6	0.1	0.4	1	0.4	0.5	0.5	1	0.4	0.1	0.6	0	0.6	0.8	0.4877	0.2688	0.3313
	2	0.7	0.4	0.7	0.1	0.8	0	0.8	0	0	0.6	0	0.6	0	0.5	0.6	1	0.42	0.0875	0.3313
	3	1	0.9	0.4	0.2	0.7	1	0	0.3	0.8	0.7	0.2	0.4	0.7	0	0.6	1	0.543	0.2188	0.4
	4	0	0.2	0	0.7	0.9	1	0.9	0.6	1	0	0	0.3	0.8	0.4	0.7	1	0.521	0.1813	0.3688
	5	0.5	0.2	0.7	0.4	0.1	0.9	0.3	0.4	0	0.4	0.1	0.2	0.3	0.5	0.6	0.6	0.3864	0.3438	0.3375
	6	0.9	0	0.9	0.5	0	1	0.9	0.3	0	0.7	0.4	0	0	0.9	0	1	0.4683	0.1375	0.3938
	7	0	0	0.9	0	0.6	0	0.4	0.7	0.9	0	0.3	0	0.8	0	0.8	1	0.3952	0.2375	0.3313
	8	0	0.7	0.9	0.7	0.7	1	0	0.6	0	0.9	0.7	0	0.8	0.6	0.8	0	0.525	0.2438	0.3813
	9	0.6	0.8	0.9	0.4	0.2	1	0.6	0	0.7	0	0.6	0	0.7	0.7	0	0	0.4554	0.1438	0.4250
Avg.	0.5	0.35	0.68	0.34	0.44	0.79	0.5	0.42	0.44	0.43	0.31	0.21	0.54	0.41	0.56	0.64	0.47007	0.2031	0.2719	
Std. dev.	0.3742	0.3408	0.2898	0.2459	0.3438	0.4175	0.3367	0.2741	0.4088	0.4029	0.2378	0.2283	0.3204	0.3143	0.3134	0.4600	0.0552	0.0746	0.0375	

Table 29. Per Category Accuracy of Std_A for Texture-shape Tests

Data Sets		stylized data																edge data		filled data
Model	Runs	airplane	bear	bicycle	bird	boat	bottle	car	cat	chair	clock	dog	elephant	keyboard	knife	oven	truck	Acc.	Acc.	Acc.
Std_{T5}	0	0.8	0.4	0	0.8	0.6	1	0.9	0.3	0.3	0	0.8	0	0	0	0	0	0.3700	0.1250	0.325
	1	0.9	0.1	0.7	0.5	0.7	0.9	0.3	0.1	0.5	0.9	0.6	0.7	0	0	0.8	0.8	0.5228	0.1688	0.3875
	2	1	0	0	0.8	0.8	0	0.6	0	0.4	0.9	0	0.7	0.8	0	0	0	0.3679	0.1625	0.2625
	3	0	0.2	1	0.2	0.1	0	0	0.8	0	0.9	0.4	0	0.9	0.4	0.9	1	0.4216	0.1438	0.2688
	4	0.8	0	0	0	0.1	1	0.7	0	0	0	0.1	0.9	0.7	0.7	0.4	0	0.3460	0.1438	0.2813
	5	0.6	0.6	0	0.7	0	0	0	0.8	0.8	0.9	0.2	0	0.8	0.7	0.8	1	0.4937	0.1813	0.3438
	6	0.8	0.4	0.6	0.5	0.7	0	0.8	0.8	0.6	1	0.8	0	0.6	0	0.3	0.8	0.5409	0.1250	0.3750
	7	0	0	0.8	0.6	0	1	0	0	0.7	0.9	0.5	0	0.9	0	0.7	0	0.3812	0.1750	0.3375
	8	0.5	0.8	0.6	0.4	0.6	0.6	0.9	0.4	0.3	0.7	0.3	0.7	0.5	0.3	0.9	0	0.5313	0.2313	0.4438
	9	0.7	0	0	0.7	0.4	0	0.7	0.6	0.5	0.9	0.3	0.9	0	0	0.6	0.8	0.4442	0.1188	0.2813
Avg.	0.61	0.25	0.37	0.52	0.4	0.45	0.5	0.38	0.41	0.71	0.4	0.39	0.52	0.21	0.54	0.44	0.4420	0.1575	0.3306	
Std. dev.	0.3510	0.2877	0.4057	0.2616	0.3197	0.4882	0.3916	0.3490	0.2685	0.3814	0.2749	0.4175	0.3795	0.2961	0.3471	0.4695	0.0753	0.0341	0.0593	

Table 30. Performance Comparison of Texture-shape Models

Models	Parameters	Cost (s/epoch)	Acc.
Std_{T5}	11840	0.387	0.442
Ort_{T5}	11840	0.407	0.470
RR_{T5}	11840	0.627	0.547
$RR_{T5} - reduced$	8044	0.552	0.483